

Gaia EDR3 comparative study of protoplanetary disk fractions in young stellar clusters

I. Mendigutía¹, E. Solano^{1,2}, M. Vioque^{3,4}, L. Balaguer-Nuñez⁵, A. Ribas⁶, N. Huélamo¹, and C. Rodrigo^{1,2}

¹Centro de Astrobiología (CAB), CSIC-INTA, Camino Bajo del Castillo s/n, 28692, Villanueva de la Cañada, Madrid, Spain.

²Spanish Virtual Observatory

³Joint ALMA Observatory, Alonso de Córdova 3107, Vitacura, Santiago 763-0355, Chile

⁴National Radio Astronomy Observatory, 520 Edgemont Road, Charlottesville, VA 22903, USA

⁵Institut de Ciències del Cosmos, Universitat de Barcelona (IEEC-UB), Martí i Franquès 1, E-08028 Barcelona, Spain

⁶European Southern Observatory (ESO), Alonso de Córdova 3107, Vitacura, Casilla 19001, Santiago de Chile, Chile

Received January 18, 2022; accepted June 5, 2022

ABSTRACT

Context. The lifetime of protoplanetary disks around young stars limits the timescale when planets form. A disk dissipation timescale ≤ 10 Myr was inferred from surveys counting the relative number of stars with disks -the disk fraction- in young stellar clusters with different ages. However, most previous surveys focused on the compact region within ~ 2 pc from the clusters' centers, for which the disk fraction information considering the outer part is practically absent.

Aims. We aim to test if disk fraction estimates change when inferred from an extended region around the clusters' centers.

Methods. Gaia EDR3 data and a best-suited, Virtual Observatory (VO)-based tool -*Clusterix*-, are used to identify member stars for a representative sample of 19 young stellar clusters considering two concentric fields of view (FOV) with radii ~ 20 pc and ~ 2 pc. Inner-disk fractions associated to each FOV are identically derived from 2MASS color-color diagrams and compared to each other.

Results. Although the density of members is smaller in the periphery, the absolute number of member stars is typically ~ 5 times larger outside ~ 2 pc from the clusters' centers. In turn, our analysis reveals that the inner disk fractions inferred from the compact and the extended regions are equal within $\sim \pm 10\%$. A list of member and disk stars identified in each cluster is provided and stored in a VO-compliant archive, along with their membership probabilities, angular distances to the centre, Gaia and near-infrared data. Averaged values and plots characterizing the whole clusters are also provided, including HR diagrams based on Gaia colors and absolute magnitudes for the sources with known extinction.

Conclusions. Our results cover the largest fields ever probed when dealing with disk fractions for all clusters analysed, and imply that their complete characterization requires the use of wide FOVs. However, the comparative study does not support a previous hypothesis proposing that disk fractions should be significantly larger considering extended regions. The resulting database is a benchmark for future detailed studies of young clusters, whose disk fractions must be accurately determined by using multi-wavelength analysis potentially combined with data from coming Gaia releases.

Key words. (Galaxy:) open clusters and associations: general – Protoplanetary disks – Proper motions – Parallaxes – Virtual observatory tools – Astronomical databases

1. Introduction

Planets form from protoplanetary disks surrounding pre-Main Sequence (PMS) stars. Thus, the lifetime of such disks constitutes a stringent upper limit to the timescale when planets assemble. The typical disk dissipation timescale is inferred by surveying young stellar clusters in order to account for the ratio between the number of stars with disks and the total number of members -the disk fraction-. Based on the observed temporal decay of the disk fraction, less than $\sim 10\%$ of stars retain their disks after 2-6 Myr and almost all stars are diskless after ~ 10 Myr (e.g. Haisch et al. 2001; Hernández et al. 2008; Mamajek 2009; Muzerolle et al. 2010; Fedele et al. 2010; Ribas et al. 2015).

However, the previous surveys are limited by the narrow field of view (FOV) of the telescopes used -mainly Spitzer. Being focused on the compact regions within $\sim 15'$, they sample the central 2-3 pc at the typical distances to the clusters, with little information about the outer parts. Indeed, although the above mentioned numbers characterizing the disk dissipation timescale are

widely accepted, they are not free of some controversial. For instance, they make our own planetary system somewhat an exception. Based on meteoritic analysis, Jupiter accreted a significant amount of gas along more than 4 Myr, similar to the timescale when the gas in the solar protoplanetary disk dissipated (see e.g. Desch et al. 2018; Schiller et al. 2018). Moreover, the use of a narrow FOV may constitute a crucial observational bias playing a fundamental role in our general understanding of disk dissipation. Pfalzner et al. (2014) suggested that the use of wide FOVs should lead to disk fractions significantly larger than inferred in previous surveys that focused on the central regions of the clusters, indicating that $\geq 50\%$ of stars should have disks at ages of ~ 10 Myr. The reason for this strong discrepancy with respect to the normally accepted disk dissipation timescale is mainly based on the assumption that young clusters significantly expand during the first Myr. In particular, the use of relatively small FOVs to survey clusters that have already expanded after $\sim 2-3$ Myr allows us to probe only the stars initially located in the central, densest regions of the clusters. A large stellar density would in

turn cause strong interactions leading to disk fractions smaller than if the stars located in periphery are also considered.

The Gaia mission (Gaia Collaboration et al. 2016) is providing a new view of stellar clusters thanks to accurate proper motions and parallaxes not limited to narrow fields or specific star forming regions. In particular, Gaia’s data have served to confirm previous suggestions indicating that most clusters expand during the critical period of disk dissipation (Kuhn et al. 2019), showing that their sizes can be much larger than previously assumed (e.g. Großschedl et al. 2021; Meingast et al. 2021). Under this new perspective, it is worth testing whether disk fraction estimates depend on the use of different FOVs or not, given its potential implications in our view of planet formation and our own planetary system. This work aims to use Gaia EDR3 data to compare the relative disk fractions of a representative sample of young stellar clusters when those are inferred considering two very different fields, compact and extended, around the center of each cluster. Section 2 details the scope and the methodology. Section 3 describes the results of this work, which are critically discussed in Sect. 4. Finally, Sect. 5 includes some concluding remarks.

2. Scope and Methodology

Our aim is to test whether sampling fields with different sizes around the center of stellar clusters lead to significantly different disk fraction estimates or not. To this end, a sample of 19 young, nearby clusters listed in Table 1 has been analysed. In particular, the vast majority of the stellar population within each cluster is in the PMS phase, and 15 out of the 19 clusters are closer than 1.5 kpc. In addition, all them were studied in previous reference works dealing with the typical disk dissipation timescale (based on relatively compact FOVs), and show a range of properties in terms of stellar masses, densities, and cluster expansion.

Because this work is based on stellar members identified through kinematic and spatial segregation using large regions around the clusters’ centers (Sect. 2.1), those clusters that cannot be unambiguously distinguished from each other were discarded. Thus, the clusters studied are separated by a wide enough angular distance, showing clearly different distances and proper motions otherwise (e.g. NGC 1333 and IC 348). This leaves well known regions such as the Orion Nebula Cluster and σ Ori excluded from the analysis. Indeed, the separation between the previous clusters is relatively small, showing very similar distances and proper motions likely indicating a physical relation (Kuhn et al. 2019; Großschedl et al. 2021).

It is also out of the scope of this work to derive accurate numbers representing absolute disk fractions for each cluster (see e.g. the references in Col. 2 of Table 1). Instead, the comparison between relative disk fractions estimated from two concentric fields with very different sizes but using identical methodology is enough for our purposes. Such a methodology is described next, and its associated caveats and limitations are discussed in Sect. 4.

2.1. Searching for member candidates

The Virtual Observatory (VO) compliant tool *Clusterix 2.0*¹ was used to find member candidates for each cluster. This is an interactive tool that determines membership probabilities using a fully non-parametric method based on proper motions. Clusterix

carries out an empirical determination of the frequency functions from the vector point diagram without previous assumptions about their profiles. The complete description and performance of Clusterix are included in Balaguer-Núñez et al. (2020).

Clusterix was applied to the stars within a circular field centered on each cluster and radius equivalent to ~ 20 pc at the corresponding distances. This radius covers the large area potentially having sources unaffected by stellar interactions after cluster expansion, eventually showing larger disk fractions than in the compact area with radius ~ 2 pc covered by most previous surveys (see Pfalzner et al. 2014, and references in Table 1). Both previous areas are different by a factor 100, will be called FOV_{20pc} and FOV_{2pc} hereafter, and are analysed independently.

Gaia EDR3 (Gaia Collaboration et al. 2021) stellar magnitudes (Riello et al. 2021), parallaxes and proper motions (Lindgren et al. 2021) were used for all stars. Only the ones with magnitude $G \leq 17$ were considered, given that the accuracy of their proper motions is the best currently possible (up to ~ 0.01 mas yr^{-1}). Such a magnitude limit constraints the minimum stellar mass that can be probed, which increases as the clusters are further away. For instance, the smallest MS stellar mass that could be probed at the distance of the furthest cluster (~ 2814 pc; NGC 1893) is $\sim 1.0 M_{\odot}$, whereas for the closest one (~ 291 pc; NGC 1333) goes down to $\sim 0.4 M_{\odot}$. The previous limits are larger as extinction increases and smaller for younger sources, thus strictly depending on the specific cluster. Nevertheless, the lack of stellar mass completeness should not significantly affect the intra-cluster comparison carried out here (but see Sect. 4.1.2). In addition, only the sources with parallax > 0 , relative parallax error < 0.1 , and renormalised unit weight error (RUWE) < 1.4 were taken into account. This way the sources with potentially spurious parallaxes are excluded and the presence of unresolved binaries minimized (Lindgren et al. 2021; El-Badry et al. 2021).

The stars whose proper motion-based membership probability is null according to Clusterix were discarded. Then, the stars whose parallax is not consistent with that associated to the cluster $\pm 3\sigma$ (being σ the Gaia-based standard deviations in Cantat-Gaudin & Anders 2020) were filtered out. Finally, potential sources showing proper motions different from the median by more than 3 times the standard deviation were considered outliers and removed from the analysis too. In short, members were identified based on kinematic segregation from proper motions, which have associated a non-null membership probability given by Clusterix, and spatial segregation from parallaxes. These criteria were equally applied to all clusters, allowing a direct comparison between the results obtained from the extended region (FOV_{20pc}) with those from the compact region within it (FOV_{2pc}). Additional filtering was applied to remove potential contamination by non-members (Sect 4.1).

2.2. Estimating inner disk fractions

A near-infrared (IR) H-K vs J-H diagram based on 2MASS photometry (Skrutskie et al. 2006) was built for the members in each cluster to estimate the disk fractions associated to FOV_{20pc} and FOV_{2pc} . JHK photometry within $2''$ from the Gaia coordinates of each member were filtered by discarding magnitudes without errorbars and colors with errorbars > 0.5 magnitudes. Members were classified as disk sources when they show $J-H < -0.007 + 1.698 \times H-K$, $J-H > 0.20$, and $H-K > 0.35$ (e.g. Lada & Adams 1992). For a given cluster and FOV, the disk fraction is $f_{disk}^{JHK} = 100 \times (N_{disk}^{JHK} / N_{memb}^{JHK})$, where N_{memb}^{JHK} and N_{disk}^{JHK} are the total number of member stars within the FOV with JHK photometry and

¹ <http://clusterix.cab.inta-csic.es/clusterix/>

Table 1: General properties of the young stellar clusters

Name	References	Age	Massive?	Expanding?	distance	Σ_{2pc}	Σ_{20pc}
...	...	[Myr]	(y/n)	(y/n)	[pc]	$[\times 10^{-2} \text{arcmin}^{-2}]$	$[\times 10^{-2} \text{arcmin}^{-2}]$
NGC 1333	^{1 2 3 4 5 6}	0-2	n	n	291±7	1.6	0.052
IC 348	^{1 2 3 4 5 6 7 8}	0-5	n	n	314±8	5.4	0.12
NGC 1893	⁶	1-2	n	y	2814±302	80	5.9
λ Ori	^{1 2 4 5 6}	1-11	n		393±8	6.2	0.37
NGC 1960	⁷	15-39 ^{†1}	n		1131±37	100	2.4
NGC 2169	⁸	6-12	n		943±43	17	0.67
NGC 2244	^{1 3 4 6}	0-4	y	y	1414±85	57	6.8
NGC 2264	^{1 2 4 6 7}	0-6	n	n	711±32	31	1.0
NGC 2353	⁸	8-16	n		1187±122	80	4.8
NGC 2362	^{1 2 3 4 6 7 8}	0-6	y	n	1271±88	110	5.8
γ Vel	^{1 2 4 6}	0-16	n		359±19	9.7	0.80
ASCC 58	⁸	7-13*	n		470±15	3.5	0.35
Tr 15	⁴	4-12	y? ^{†2}	y?	2358±261	440	40
NGC 6231	^{6 8}	1-9	y	n	1588±115	230	15
NGC 6531	⁸	5-10	n		1214±68	96	7.4
NGC 6611	^{4 6}	1-4	y	y	1602±126	150	16
Tr 37	^{1 2 3 4 6}	0-6	y ^{†3}		914±32	31	2.3
NGC 7129	^{1 2 3 4 6}	0-6	n		915±56	12	0.38
NGC 7160	^{1 2 3 4 8}	8-15	n	n	920±48	17	1.2

Notes: Column 2 lists disk dissipation studies where the clusters in Col. 1 were included. The numbers in Cols 3 and 4 are based on such studies and references therein. The age range is indicated in Col. 3. Following Mamajek (2009), an uncertainty of 30% has been assigned to ages without errorbars. Column 4 indicates whether the cluster has a total stellar mass above or below 500-1000 M_{\odot} (yes or not), which is in turn indicative of the presence of a significant number of massive OB stars within the clusters (but note that most are part of OB associations when larger scales are considered; see e.g. Wright 2020). The presence or absence of evidence indicating cluster expansion (yes or not) is indicated in Col. 5, whenever available in Kuhn et al. (2019). The last three columns are based on our work. The average Gaia EDR3 distance (and standard deviation) to each cluster is shown in Col. 6 (see Appendix C). Columns 7 and 8 show the surface density of member stars for the inner FOV_{2pc} and the whole FOV_{20pc}, as inferred from Table A.1. **References:** ¹Hernández et al. (2008), ²Mamajek (2009), ³Muzerolle et al. (2010) ⁴Pfalzner et al. (2014), ⁵Ribas et al. (2015), ⁶Guarcello et al. (2021), ⁷Haisch et al. (2001), ⁸Fedele et al. (2010). ^{†1}Panja et al. (2021), ^{†2}Wang et al. (2011) ^{†3}Saurin et al. (2012).

the corresponding number of stars classified as disks sources, respectively. Errorbars for the disk fractions were derived from the different N_{disk}^{JHK} values associated to the colors' uncertainties.

Alternative diagrams based on IRAS, AKARI, or Spitzer colors and magnitudes are commonly used to identify disk sources. Nevertheless, they are not ideal for our comparison purposes because their coverage is partial or limited to compact regions around the center of most clusters analyzed here. The situation is similar using the more complete all-sky WISE survey, once potentially spurious magnitudes are filtered out (Koenig & Leisawitz 2014). In contrast, the 2MASS survey typically covers more than 90% of the identified members within both FOV_{20pc} and FOV_{2pc} simultaneously. This allows us to carry out a statistically significant comparison between the disk fractions inferred from the corresponding color-color diagram for all clusters and FOVs, guarantying that the inevitable exclusion of the few members without JHK counterparts has no major effect. It is remarked that the near-IR photometry used in this work allows us to identify sources with hot inner disks at distances $\lesssim 1$ au from the central star, but not colder disks at longer distances. The caveats and limitations associated to the JHK color-color diagram are discussed in more detail in Sect. 4.2.

3. Results

Appendix A includes the figures and tables summarizing the results. The distributions of stars in the proper motion plane and the projected directions of motion of all members identified in each cluster are shown in Figs. A.1 and A.2. Their on-sky positions and the sizes of the compact and the extended FOVs are overplotted to an image of the region in the IR in Fig. A.3. The JHK color-color diagrams used to infer the inner disk fractions are in Figure A.4. Additionally, Fig. A.5 shows the Gaia color-magnitude diagram of each cluster, although its representativeness depends on how well the extinction is characterized (see the legends in that figure and Sect. 4.1). Table A.1 lists the central coordinates of each cluster, along with the angular radius, fraction of members identified with respect to the field stars, mean parallaxes and proper motions derived using FOV_{20pc} and FOV_{2pc}. Table A.2 lists the Gaia EDR3 coordinates, proper motions, parallax, and magnitudes, as well as the angular distance to the center, membership probability and 2MASS colors -when available- of all member stars. Disk stars identified through the procedure described in Sect. 2.2 are indicated. Finally, a VO-compliant archive where all previous data are available is described in Appendix B, and a comparison with previous Gaia-based results is in Appendix C. Next we focus on the main results that will be analysed in this work.

Firstly, although the surface density of members closer than 2 pc is larger than that further out by a factor ranging from ~ 10

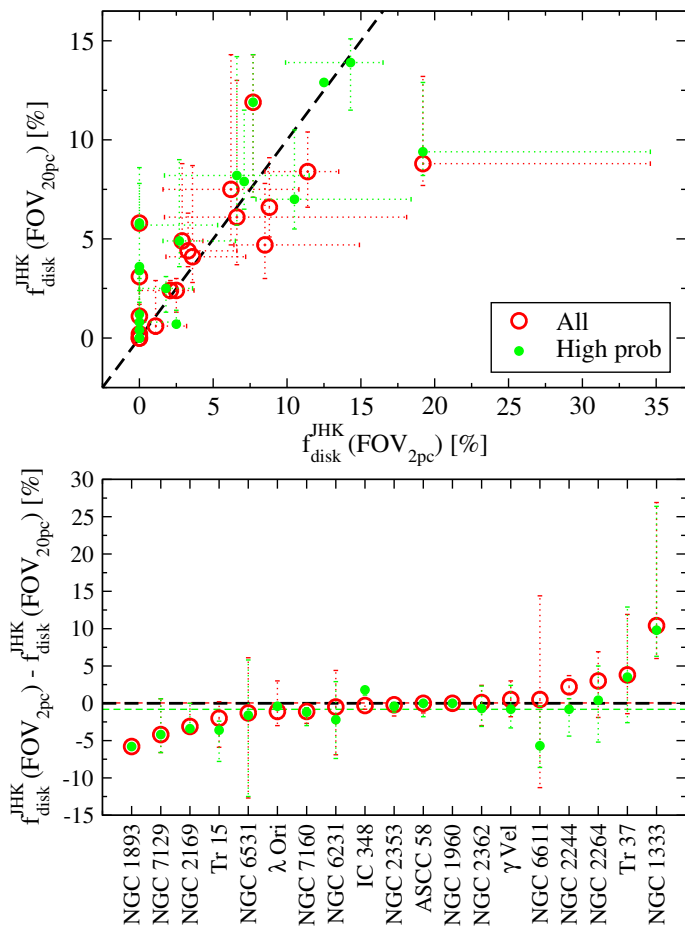


Fig. 1: Inner disk fractions from the compact and extended regions are plotted against each other in the top panel, and their differences in the bottom panel. The red and green circles are results based on all members identified per cluster or on the high-probability members, respectively. The black dashed lines indicate equal values in both panels, and the mean differences are shown in the bottom panel with red and green dashed lines.

to 86 (typically ~ 28 on average), the absolute number of members in the periphery can be up to ~ 11 (typically ~ 5) times larger. Thus, the number of members associated to clusters significantly differs from previous surveys focused on narrow FOVs within the first ~ 2 pc, which need to be updated to better account for the whole stellar populations. On the other hand, Cols 3 and 7 of Table 2 list the inferred disk fractions associated to each cluster and FOV, whose representativeness is quantified in Cols. 2 and 6 showing the fraction of member stars with JHK photometry. Figure 1 compares the disk fractions derived using FOV_{2pc} versus those derived using FOV_{20pc} , illustrating their similarity. The difference between both is below errorbars in most clusters, typically smaller than $\sim {}_{-5}^{+10}$ %, and with a mean value = 0.05%. Considering errorbars, the difference between disk fractions can reach ${}_{-13}^{+14}$ % (except for NGC 1333). Thus, based on this analysis the use of a large FOV does not lead to disk fractions significantly larger than those inferred from compact regions around the clusters' centers, in contrast with the proposal in Pfalzner et al. (2014). The previous results are critically discussed next.

4. Analysis and discussion

4.1. Consistency

4.1.1. Potential contamination

A proper comparison between disk fractions requires that potential contamination by non-members equally affects the samples within FOV_{2pc} and outside that region. One way to assess this requirement is by having equivalent distributions of membership probabilities for the members identified within FOV_{2pc} and for the rest. Two-sample Kolmogorov-Smirnov (KS) tests were applied to both previous sub-samples in each cluster. The p-value inferred from the KS tests is < 0.05 for most clusters, rejecting the hypothesis that the membership probabilities are drawn from the same parent distribution. The reason explaining those cases is that whereas most FOV_{2pc} members have membership probabilities above a certain value, the rest of the members located further away have membership probabilities both above and below that value. Filtered samples with membership probabilities above a threshold were built, increasing such a threshold until the KS test provided a p-value > 0.05 . The p_0 values defining the membership probability thresholds from which the KS tests support that the member sub-samples are drawn from the same parent distribution are indicated in Table 2. Considering a more stringent membership probability $> p_0$ (instead of > 0) results in a significantly reduced number of members outside 2 pc, whereas the sample within FOV_{2pc} remains comparatively unaltered in most clusters (see Cols. 2, 4 and 6, 8 in that table).

An example illustrating the previous procedure is shown in Fig. 2. Membership probabilities are plotted against the angular distance to the center of NGC 6231, which is the cluster with the largest number of members identified in this work. Although the membership probabilities assigned by Clusterix only rely on proper motions, the members within 2 pc tend to show comparatively large probabilities, which is not the case for many sources that are further away. The observed difference in the probability distributions is confirmed by the KS test, revealing that such a difference is present until a membership probability threshold $p_0 = 0.7$ is reached. Thus, in order to make a comparison addressing potentially uneven contamination in NGC 6231, disk fractions must be modified by only considering the stars with a membership probability > 0.7 . The high-probability members within 2 pc represents 81% of all members initially identified in that region. In contrast, only 34% of the members initially identified outside 2 pc are now considered.

Modified disk fractions in Cols. 5 and 9 of Table 2 are compared in Fig. 1 (green circles). The result obtained in Sect. 3 based on complete member samples is supported when only the high-probability members are considered. The difference between disk fractions inferred from the compact and extended FOVs is again $\sim {}_{-5}^{+10}$ %, mostly within ~ 13 % even considering errorbars, and the typical (mean) difference is similar too (-0.8%). The comparison between disk fractions in clusters with low p_0 values (e.g. NGC 1333, NGC 7160) does not change significantly if more stringent probability cuts are used, although the statistical significance is reduced because of the smaller sample sizes.

The previous test supports that if some differential contamination is present this does not significantly affect the result concerning the comparison between disk fractions. Indeed, the mean proper motions inferred from all members within FOV_{2pc} and FOV_{20pc} are equal considering errorbars for all clusters (Table A.1), and consistent with previous Gaia-based determinations using narrower FOVs (Appendix C). The direction of motion of

Table 2: Class II inner disk fractions from 2MASS color-color diagrams

Name	FOV _{20pc}				FOV _{2pc}			
	N_{JHK}/N_{memb}	f_{disk}^{JHK}	N_{JHK}/N_{memb} (p_0)	f_{disk}^{JHK} (p_0)	N_{JHK}/N_{memb}	f_{disk}^{JHK}	N_{JHK}/N_{memb} (p_0)	f_{disk}^{JHK} (p_0)
NGC 1333	91/95	$8.8^{+4.4}_{-1.1}$	85/88 (0.2)	$9.4^{+3.5}_{-1.2}$ (0.2)	26/28	$19.2^{+15.4}_{-0.0}$	26/28 (0.2)	$19.2^{+15.4}_{-0.0}$ (0.2)
IC 348	205/209	$2.4^{+0.5}_{-0.0}$	148/151 (0.6)	$0.7^{+0.7}_{-0.0}$ (0.6)	95/97	$2.1^{+0.0}_{-0.0}$	81/83 (0.6)	$2.5^{+0.0}_{-0.0}$ (0.6)
NGC 1893	52/59	$5.8^{+0.0}_{-0.0}$	52/59 (0.5) [†]	$5.8^{+0.0}_{-0.0}$ (0.5) [†]	7/8	$0.0^{+0.0}_{-0.0}$	7/8 (0.5) [†]	$0.0^{+0.0}_{-0.0}$ (0.5) [†]
λ Ori	366/377	$4.4^{+1.9}_{-0.8}$	31/31 (0.9)	$12.9^{+0.0}_{-0.0}$ (0.9)	61/63	$3.3^{+3.3}_{-0.0}$	16/16 (0.9)	$12.5^{+0.0}_{-0.0}$ (0.9)
NGC 1960	265/273	$0.0^{+0.0}_{-0.0}$	243/250 (0.8)	$0.0^{+0.0}_{-0.0}$ (0.8)	109/114	$0.0^{+0.0}_{-0.0}$	106/110 (0.8)	$0.0^{+0.0}_{-0.0}$ (0.8)
NGC 2169	98/102	$3.1^{+0.0}_{-0.0}$	59/62 (0.9)	$3.4^{+0.0}_{-0.0}$ (0.9)	23/26	$0.0^{+0.0}_{-0.0}$	21/23 (0.9)	$0.0^{+0.0}_{-0.0}$ (0.9)
NGC 2244	407/418	$6.6^{+2.5}_{-1.5}$	140/147 (0.9)	$7.9^{+3.6}_{-1.4}$ (0.9)	34/35	$8.8^{+0.0}_{-0.0}$	28/28 (0.9)	$7.1^{+0.0}_{-0.0}$ (0.9)
NGC 2264	441/452	$8.4^{+2.0}_{-1.8}$	165/166 (0.8)	$13.9^{+1.2}_{-2.4}$ (0.8)	140/142	$11.4^{+2.1}_{-2.9}$	91/91 (0.8)	$14.3^{+2.2}_{-4.4}$ (0.8)
NGC 2353	530/545	$0.2^{+1.5}_{-0.2}$	236/243 (0.8)	$0.4^{+0.8}_{-0.4}$ (0.8)	87/92	$0.0^{+0.0}_{-0.0}$	75/80 (0.8)	$0.0^{+0.0}_{-0.0}$ (0.8)
NGC 2362	461/485	$2.4^{+0.6}_{-0.2}$	162/170 (0.9)	$2.5^{+0.6}_{-0.2}$ (0.9)	80/90	$2.5^{+1.2}_{-0.0}$	56/63 (0.9)	$1.8^{+1.8}_{-0.0}$ (0.9)
γ Vel	780/810	$0.6^{+2.3}_{-0.4}$	399/415 (0.5)	$0.8^{+1.2}_{-0.5}$ (0.5)	94/99	$1.1^{+2.5}_{-0.0}$	74/78 (0.5)	$0.0^{+2.7}_{-1.8}$ (0.5)
ASCC 58	150/160	$0.0^{+1.3}_{-0.0}$	112/118 (0.5) [†]	$0.0^{+0.0}_{-0.0}$ (0.5) [†]	14/16	$0.0^{+0.0}_{-0.0}$	13/15 (0.5) [†]	$0.0^{+0.0}_{-0.0}$ (0.5) [†]
Trumpler 15	738/870	$4.9^{+3.9}_{-0.8}$	167/207 (0.8)	$3.6^{+4.2}_{-0.2}$ (0.8)	70/94	$2.9^{+1.4}_{-0.0}$	34/49 (0.8)	$0.0^{+0.0}_{-0.0}$ (0.8)
NGC 6231	1477/1726	$4.1^{+4.6}_{-1.3}$	616/714 (0.7)	$4.9^{+4.1}_{-1.7}$ (0.7)	225/265	$3.6^{+3.6}_{-0.0}$	183/214 (0.7)	$2.7^{+3.8}_{-0.0}$ (0.7)
NGC 6531	469/696	$7.5^{+6.8}_{-2.3}$	282/404 (0.6)	$8.2^{+6.0}_{-2.5}$ (0.6)	65/91	$6.2^{+4.6}_{-1.8}$	61/83 (0.6)	$6.6^{+4.9}_{-1.0}$ (0.6)
NGC 6611	652/809	$6.1^{+5.9}_{-2.4}$	35/45 (0.99)	$5.7^{+2.9}_{-0.0}$ (0.99)	61/72	$6.6^{+11.5}_{-4.9}$	19/23 (0.99)	$0.0^{+5.3}_{-0.0}$ (0.99)
Trumpler 37	360/381	$4.7^{+3.1}_{-1.7}$	199/216 (0.4)	$7.0^{+3.5}_{-1.5}$ (0.4)	47/52	$8.5^{+6.4}_{-2.1}$	38/43 (0.4)	$10.5^{+7.9}_{-2.6}$ (0.4)
NGC 7129	42/43	$11.9^{+2.4}_{-4.8}$	42/43 (0.5) [†]	$11.9^{+2.4}_{-4.8}$ (0.5) [†]	13/14	$7.7^{+0.0}_{-0.0}$	13/14 (0.5) [†]	$7.7^{+0.0}_{-0.0}$ (0.5) [†]
NGC 7160	185/190	$1.1^{+1.6}_{-0.5}$	171/176 (0.2)	$1.2^{+1.8}_{-0.6}$ (0.2)	27/27	$0.0^{+0.0}_{-0.0}$	27/27 (0.2)	$0.0^{+0.0}_{-0.0}$ (0.2)

Notes. Columns. 2, 3, 6 and 7: ratio between the number of members with JHK counterparts and the total number of members, and the inner disk fractions (in %) for each cluster and FOV. Rest of the columns: same values for the stars whose membership probability is above a certain threshold p_0 (indicated between parentheses). [†] p_0 values were arbitrarily set to 0.5, given that the KS test already provided a p-value > 0.05 (see Sect. 4.1.1). Listed disk fractions are valid for comparison purposes but should not be taken as absolute values, given the limitations of our study (see text).

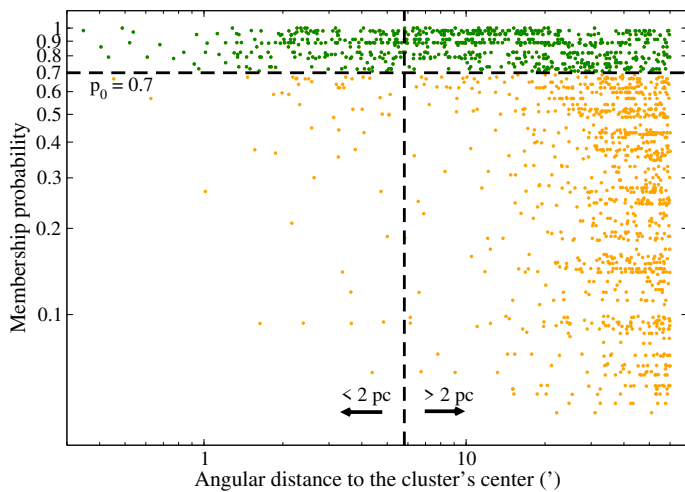


Fig. 2: Membership probability against angular distance to the center of NGC 6231 for all members identified in this cluster (log-scale). The vertical dashed line defines two sub-samples closer and further than 2 pc from the cluster’s center. The horizontal dashed line indicates the probability threshold p_0 below which the KS test rules out that the probability distributions of both previous sub-samples are drawn from the same parent distribution. The resulting high- and low-probability members are indicated with dark green and orange, respectively.

the members identified inside and outside 2 pc roughly coincides in all clusters too (Fig. A.2).

The fact that the comparison between disk fractions remains essentially unaltered after removing the potential contaminants

identified above suggests that these share a similar evolutionary stage, thus supporting that they mostly belong to the clusters too. Indeed, if a large enough number of the low-probability members -mainly located in the periphery- were e.g. MS stars, disk fractions using FOV_{20pc} should be larger once such wrongly introduced members are removed. Therefore, we should not see strong differences between the high- and low- probability members concerning their location on the HR diagram of each cluster. In order to place the members in the Gaia color-magnitude diagram (CMD hereafter), the observed BP-RP colors and G magnitudes should first be corrected from extinction. The Gaia EDR3-based optical extinction values (A_v) in Anders et al. (2022) are the most recent and complete estimates homogeneously derived, and are best suited for our purposes. Gaia intrinsic colors (BP-RP)₀ were calculated using such A_v values, the wavelength corrections from Casagrande et al. (2021), and a typical total-to-selective extinction ratio $R_v = 3.1$. Extinction-corrected absolute MG magnitudes were derived by also using the Gaia EDR3 geometrical distances to each member based on Bailer-Jones et al. (2021). Errorbars were inferred propagating the individual uncertainties in the Gaia magnitudes and parallaxes, and assigning an additional 10% error associated to extinction.

Fully representative CMDs can be built for NGC 1960, NGC 2353, ASCC 58, and NGC 6231, given that A_v values in Anders et al. (2022) are available for $\geq 90\%$ of their members. An example is shown in Fig. 3, once again focused on NGC 6231 (see Fig. 2). PARSEC isochrones and evolutionary tracks from Bressan et al. (2012) are overplotted for reference. High- and low-probability members are similarly distributed, their location in the CMD being above the Zero Age Main Sequence (ZAMS) and consistent with the PMS phase in almost all cases. The majority of the members have ages in between 1 and 10 Myr, in agreement

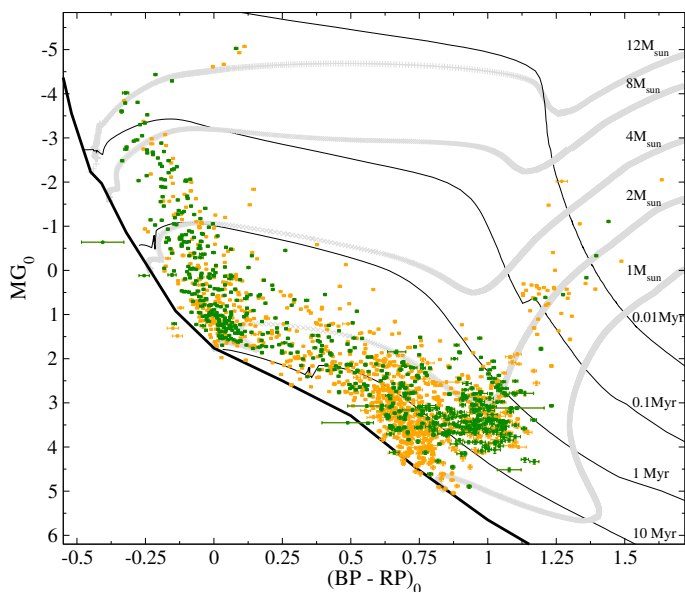


Fig. 3: Extinction corrected Gaia CMD of NGC 6231, where the high- and low- probability members are indicated with dark green and orange as identified in Fig. 2. In this case 90% and 91% of the high- and low-probability members are shown, given that extinction values are not available for the rest. The ZAMS loci is indicated with the black solid curve. PMS isochrones and evolutionary tracks are overplotted in black and gray for the stellar ages and masses indicated.

with previous estimates (Table 1). The $\sim 4\text{--}12 M_{\odot}$ and $\sim 2 M_{\odot}$ stars showing ages < 1 Myr, as well as more evolved sources, are both low- and high- probability members. Particularly, the fraction of members with extinction values that are already in the MS is the same for the low- and high-probability sub-samples, $< 0.5\%$. All previous similarities support that the vast majority of the members identified actually belong to the same cluster, explaining why the comparison between disk fractions leads to virtually the same result regardless of the use of the whole sample or the high-probability sub-sample.

The same exercise was applied to the rest of the clusters. It is noted, however, that for most of them extinction values are available only for a fraction of members $< 90\%$, being $< 50\%$ for NGC 1333, IC 348, λ Ori, NGC 2264, and NGC 7129. With the previous caveat in mind, we find no evidence indicating that the location of the high- and low- probability members in the Gaia CMDs generally differs. For this reason, and because the overall comparison between disk fractions remains essentially the same (Fig. 1), all members identified are equally considered in this work². Gaia CMDs for all clusters are included in Fig. A.5. The distinction in this figure between the FOV_{2pc} and the FOV_{20pc} members will be used in the remaining discussion.

4.1.2. Potential mass and age biases

Disk fraction studies specifically devoted to intermediate-mass young stars are not abundant, but they suggest that disk dissipation is slightly faster than that for lower-mass objects (Hernández et al. 2007; Yasui et al. 2014; Ribas et al. 2015). In addition, evolutionary studies based on disk fractions assume that all stars

² Membership probabilities are provided for all stars in each cluster in Table A.2, for which different probability cuts could be applied by the interested readers.

in a given cluster are roughly coeval (see e.g. the references in Sect. 1 and Table 1). Therefore, The interpretation of the result indicating similar disk fractions within each cluster when using FOV_{2pc} and FOV_{20pc} may depend on whether such fractions refer to stars with similar stellar masses and ages or not.

Figure 4 compares the typical (mean) extinctions of the inner and outer regions of the clusters analysed in this work, as inferred from the individual A_V values of the members from Anders et al. (2022). Errorbars reflect the corresponding standard deviations. For the majority of the clusters there is no difference between the typical extinctions within $\pm 1\sigma$. Thus, the lower mass limit that could be probed within each of the previous clusters is the same regardless of the FOV. A closer look to the Gaia CMDs (Fig. A.5) of the four clusters with the best extinction characterization (ASCC 58, NGC 1960, NGC 2353, and NGC 6231) confirms that the mass ranges probed by FOV_{2pc} and FOV_{20pc} are indeed the same within each cluster. Therefore, the comparison between the corresponding disk fractions is consistent at least concerning the stellar mass range that they represent. On the other hand, the CMDs reveal that the strongest differences between the smallest stellar mass probed through FOV_{2pc} and FOV_{20pc} are shown by NGC 1333 and IC 348, which results from the strong differential extinction between the inner and outer regions. In such cases (see also e.g. NGC 7129 and Tr 37) the innermost region probes masses $\geq 1M_{\odot}$ whereas the outer region goes down to $\sim 0.5M_{\odot}$. Although small differences in the disk dissipation timescales -and thus on disk fractions- are expected mainly when the mass ranges compared differ by a larger amount (see the references above, but also Hernández et al. 2010) these cases should be viewed with caution given the current lack of information concerning extinction.

Regarding the evolutionary stage, although the vast majority of the members identified in each cluster consistently fall within the PMS location in the CMDs, age spread is apparent in several of them. This is not surprising, based on the scatter found in the literature for the clusters in this work analysed from a variety of data and inferred from different sub-populations, as referred in Table 1. Clusters in that table with narrow age ranges like NGC 1333 are indeed mainly based on single works focused on compact regions and specific sub-samples (Wilking et al. 2004), although our data shows that an older population is also present in that cluster (see the corresponding panel in Fig. A.5). More recent Gaia-based works already find considerable age scatter in regions comparable to FOV_{2pc} for many young clusters (e.g. Getman et al. 2018; Prisinzano et al. 2019), confirming previous findings from the pre-Gaia era (e.g. Getman et al. 2014b,a; Jeffries 2017, and references therein).

Nevertheless, the comparison between disk fractions is not compromised as long as the fractions of members with different ages are similar for both FOVs. This is the case for the majority of the clusters, based on their CMDs in Fig. A.5. Following with the same representative example of NGC 6231, $\sim 85\%$ of the members have ages > 1 Myr (with 0.4% already in the MS) and the remaining $\sim 15\%$ are younger, such fractions being very similar both for the FOV_{20pc} and a FOV_{2pc} sub-samples. Then the fact that the disk fractions inferred using both FOVs are equal within errorbars can be interpreted in terms of a similar disk dissipation timescale regardless of the distance to the center of the cluster. A relevant exception is NGC 1893. The majority of the members within FOV_{2pc} have ages in between 1 and 10 Myr, but a significant fraction of the members identified in the outer region are younger than 1 Myr. This difference would explain why NGC 1893 shows a FOV_{20pc} -based disk fraction larger above errorbars than that based on FOV_{2pc} (Fig. 1). Similarly, the fact

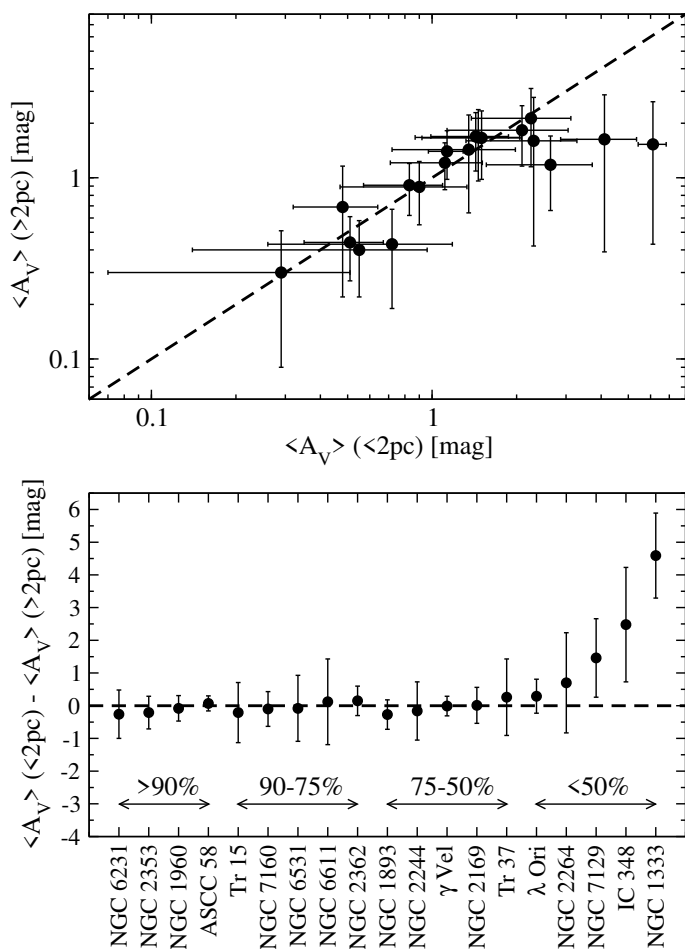


Fig. 4: Mean optical extinction from the stars located closer and further than 2 pc from the center of each cluster are plotted against each other in the top panel (log-scale), and their differences in both panels. The dashed lines indicate equal values are adopted as errorbars within each cluster are adopted as errorbars in the top panel. Uncertainties in the bottom panel are derived from the propagation of the individual 1σ deviations. The fraction of member stars for which extinction values from Anders et al. (2022) are available for each cluster is indicated above the arrows in the bottom panel.

that NGC 1333 is the other cluster showing the largest differences between the $\text{FOV}_{2\text{pc}}$ - and $\text{FOV}_{20\text{pc}}$ -based disk fractions is probably related to a significant age spread depending on the radial distance to the center. However, in this case the inner region is probably younger than the outer one. Although such an age difference is motivated by the presence of very young, embedded Class 0/I sources in the inner region of NGC 1333 (e.g. Young et al. 2015; Fiorellino et al. 2021) and the observed differential extinction (Fig. 4), that age gradient cannot be assessed solely based on its Gaia CMD. As it was mentioned before, this is barely representative given the lack of enough extinction information.

In other clusters, sub-populations with specific ages present only in $\text{FOV}_{20\text{pc}}$ are that small that their presence/absence is virtually irrelevant for the disk fraction estimate (e.g. NGC 2353). In particular, the presence of a few MS stars in the Gaia CMDs of some clusters does not affect the disk fraction comparison. Disk fractions were indeed recalculated in all cases showing such evolved sources assuming the percentages of MS stars in-

ferred from the CMDs in Fig. A.5, and that they are contaminants not belonging to the cluster. No significant difference with respect to the values already provided in Table 2 was found.

4.2. Limitations

On top of the already mentioned caveats concerning the methodology described in Sect. 2, additional limitations should be considered when the disk fractions associated to the compact and extended regions are compared to each other.

Firstly, because the departure point to identify members are the Gaia magnitudes in the optical, we are probing essentially Class II stars but not most of the embedded Class 0/I sources. Indeed, the ratio between the number of Class II and Class 0/I sources can change depending on the cluster, e.g. a factor ~ 2 in NGC 1333 or ~ 10 in IC 348 (Young et al. 2015). Thus, the inferred disk fractions are lower limits for the less evolved clusters hosting Class 0/I sources. However, embedded stars are mainly located in the densest and more extincted parts of the clusters (e.g. Gutermuth et al. 2008), which tend to be closer to the center (Fig. 4). Therefore, although the inclusion of these sources would make the absolute disk fractions larger than provided here, such an increase would be mainly related to those obtained using $\text{FOV}_{2\text{pc}}$. In this respect, accurate disk fractions based on compact regions should be upper limits to those inferred from extended FOVs, and not the other way around (Pfalzner et al. 2014).

Secondly, the use of JHK color-color diagrams allows us to identify "full" disks with IR excess starting at $\sim 1.2 - 2.2 \mu\text{m}$, but not "transitional" disks with excesses only observable at longer wavelengths. The number of transitional disks is larger in older clusters, representing around 10% to 50% of disk stars (Currie & Sicilia-Aguilar 2011; Balog et al. 2016). This again indicates that the disk fractions provided here are lower limits, in this case specially affecting the evolved clusters. However, to our knowledge there is no evidence suggesting that the location of transitional disks with respect to the center of the clusters is different than that of full disks. Assuming that transitional and full disks are similarly distributed within the clusters, our result based on the comparison between relative disk fractions inferred from the compact and the extended regions remains unaltered.

On the other hand, disk dispersal shows roughly similar timescales regardless of the wavelength or the observational tracer used (e.g. the review in Ercolano & Pascucci 2017, and references therein), but it is not clear if this applies to environmental effects that promote disk destruction. Indeed, the presence of massive stars or stellar interactions in the densest and more massive clusters may lead to a fast disappearance of the outer disk probed at sub-mm and mm wavelengths (e.g. Anderson et al. 2013; Ansdell et al. 2017; Vincke & Pfalzner 2018; van Terwisga et al. 2019). The eventual influence of such environmental effects is the subject of ongoing debate (see e.g. the discussion in Parker et al. 2021, and references therein), but it does not seem to affect the bulk of the disks probed at shorter IR wavelengths (e.g. Richert et al. 2015). Such a possible difference with the outer disk dispersal depending on the environment cannot be analysed based on the JHK photometry used in this work, which we remark again that only refers to inner dust disks.

A major limitation concerning the JHK color-color diagram is that although it is very efficient identifying inner disks around intermediate-mass Herbig Ae/Be stars, up to $\sim 30\%$ of classical T Tauri stars (TTs) may fall in the region associated to extincted MS stars, therefore remaining undetected (Lada & Adams 1992; Haisch et al. 2001; Mamajek 2009). This is not problematic for

our comparative study of disk fractions, unless the relative number of undetected TTs changes with the FOV. In particular, for certain clusters one may expect that the central regions are more extincted than further away (Fig. 4). Then the relative number of members located between the bands defining extincted MS stars in the JHK diagram should be larger within FOV_{2pc} than within FOV_{20pc} . Indeed, Fig. A.4 shows that this is the case for extincted clusters like NGC 1333, and IC 348. Consequently, the disk fractions inferred using FOV_{2pc} may significantly increase in these clusters once TTs potentially falling within the extinction region for MS stars in the JHK diagram are identified as disk stars. This is once again indicating that disk fractions inferred from FOV_{20pc} cannot generally be significantly larger than those from FOV_{2pc} , but the case is probably the opposite. Assuming the worst case scenario in which our disk fractions only account for 70% of classical TTs (i.e. $f_{disk}^{real} = f_{disk}/0.7$), the maximum differences between disk fractions estimated from both FOVs would increase from $\sim 10\%$ to $\sim 14\%$.

5. Concluding remarks

A representative sample of young clusters has been analysed aiming to compare the inner disk fractions associated to a compact and an extended region with radii ~ 2 and 20 pc from the center of each cluster. This size is larger than that probed in all previous reference surveys studying disk fractions and in more recent Gaia-based studies for the majority of the clusters. Although the density of members in the periphery is smaller than in the compact region, the absolute number is on average factor ~ 5 larger at distances further than 2 pc from the clusters' centers. This motivates future, detailed studies of young clusters including more complete samples by probing extended regions, which may affect e.g. the typical ages or the age dispersion within the clusters. Our analysis also reveals that inner disk fractions based on the extended region are not generally larger than those from the compact region by $\sim 50\%$ or more, contrasting with previous predictions (Pfalzner et al. 2014). On the contrary, the found differences are typically $\lesssim 10\%$, and none of the relatively old clusters with negligible disk fractions in the literature (NGC 1960, NGC 2169, NGC 2353, ASCC 58, Trumpler 15, and NGC 7160) shows such a significant increase when the extended region is considered.

The limitations and caveats affecting our study have been discussed in detail along the text, and must be taken into account when interpreting the previous result. Particularly relevant is that although the presence of massive stars or stellar interactions in the densest and more massive clusters may lead to a fastest disappearance of the outer disks, these cannot be probed based solely on the near-IR photometry used in this work. It is also noted that for this study we limited ourselves to a maximum radius of 20 pc from the clusters' centers, but their true extension could be significantly larger. For instance, a preliminary analysis of NGC 1333 indeed shows new members up to a radial distance of ~ 40 pc, when no additional ones are found based on proper motion analysis with Clusterix.

Multi-wavelength analysis, potentially combined with data coming from future Gaia releases -e.g. radial velocities-, are necessary to provide accurate disk fractions and better constraint the number and properties of the cluster's members. The database resulting from this work is available online and constitutes a benchmark for such detailed studies.

Acknowledgements. The authors acknowledge the anonymous referee, whose constructive suggestions have served to improve the manuscript. IM, ES, LBN, NH, and CR acknowledge support by the Spanish

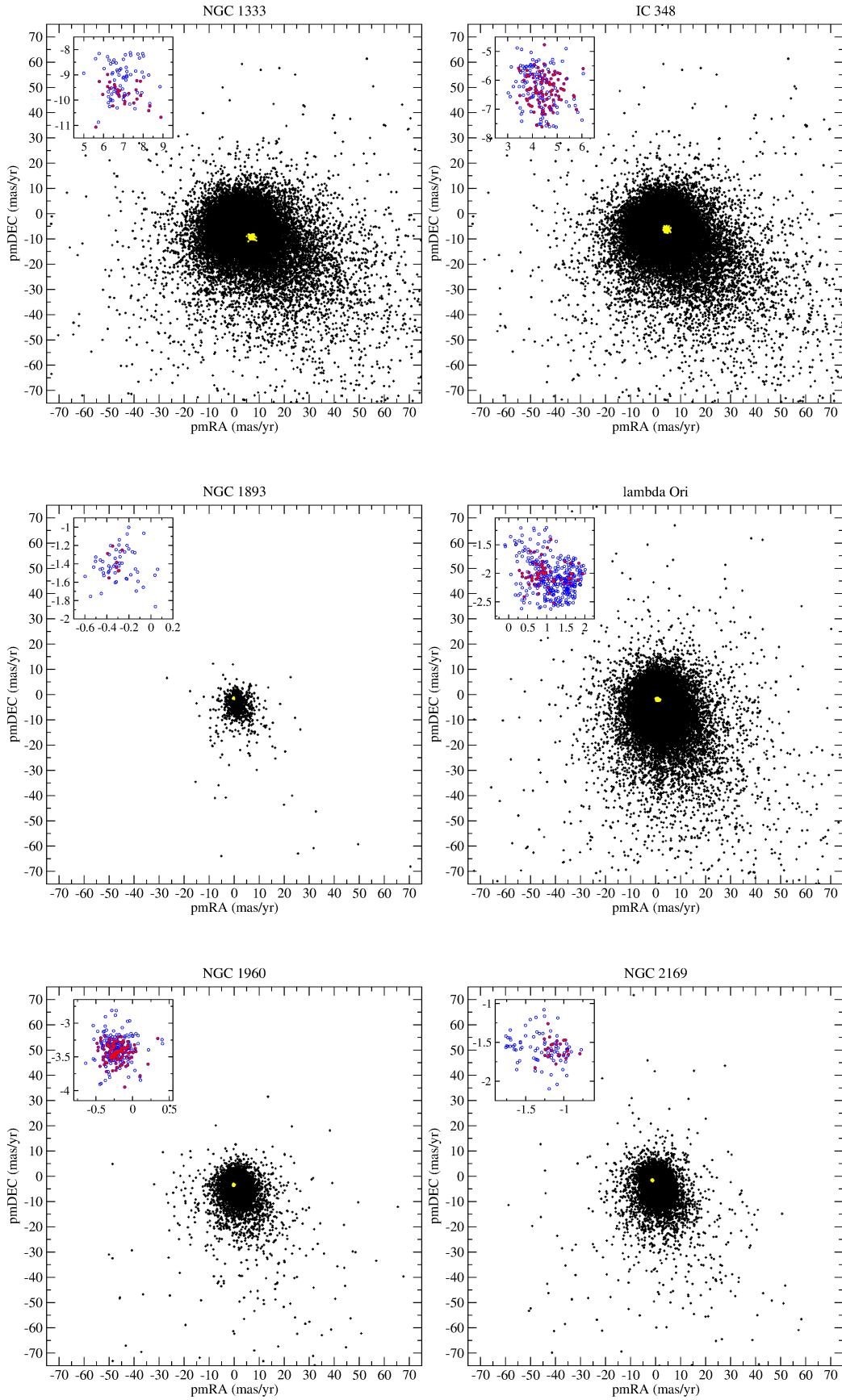
MICIN/AEI/10.13039/501100011033. IM, ES, NH, and CR are partially funded by MDM-2017-0737 Unidad de Excelencia *María de Maeztu* - Centro de Astrobiología (CSIC-INTA). IM is funded by a RyC2019-026992-I grant. ES has been funded through grant PID2020-112949GB-I00. LBN acknowledges support by "ERDF A way of making Europe" by the "European Union" through grant RTI2018-095076-B-C21, and the Institute of Cosmos Sciences University of Barcelona (ICCUB, Unidad de Excelencia "María de Maeztu") through grant CEX2019-000918-M. NH has been partially funded by the AEI Project ESP2017-87676-C5-1-R. This research is based on Clusterix 2.0 service at CAB (INTA-CSIC), and has made extensive use of TOPCAT (Taylor 2005). This work has made use of data from the European Space Agency (ESA) mission *Gaia* (<https://www.cosmos.esa.int/gaia>), processed by the *Gaia* Data Processing and Analysis Consortium (DPAC, <https://www.cosmos.esa.int/web/gaia/dpac/consortium>). Funding for the DPAC has been provided by national institutions, in particular the institutions participating in the *Gaia* Multilateral Agreement. This publication makes use of data products from the Two Micron All Sky Survey and the Wide-field Infrared Survey Explorer, which are joint projects of the University of Massachusetts and the Infrared Processing and Analysis Center/California Institute of Technology; and the University of California, Los Angeles, and the Jet Propulsion Laboratory/California Institute of Technology, funded by the National Aeronautics and Space Administration and the National Science Foundation.

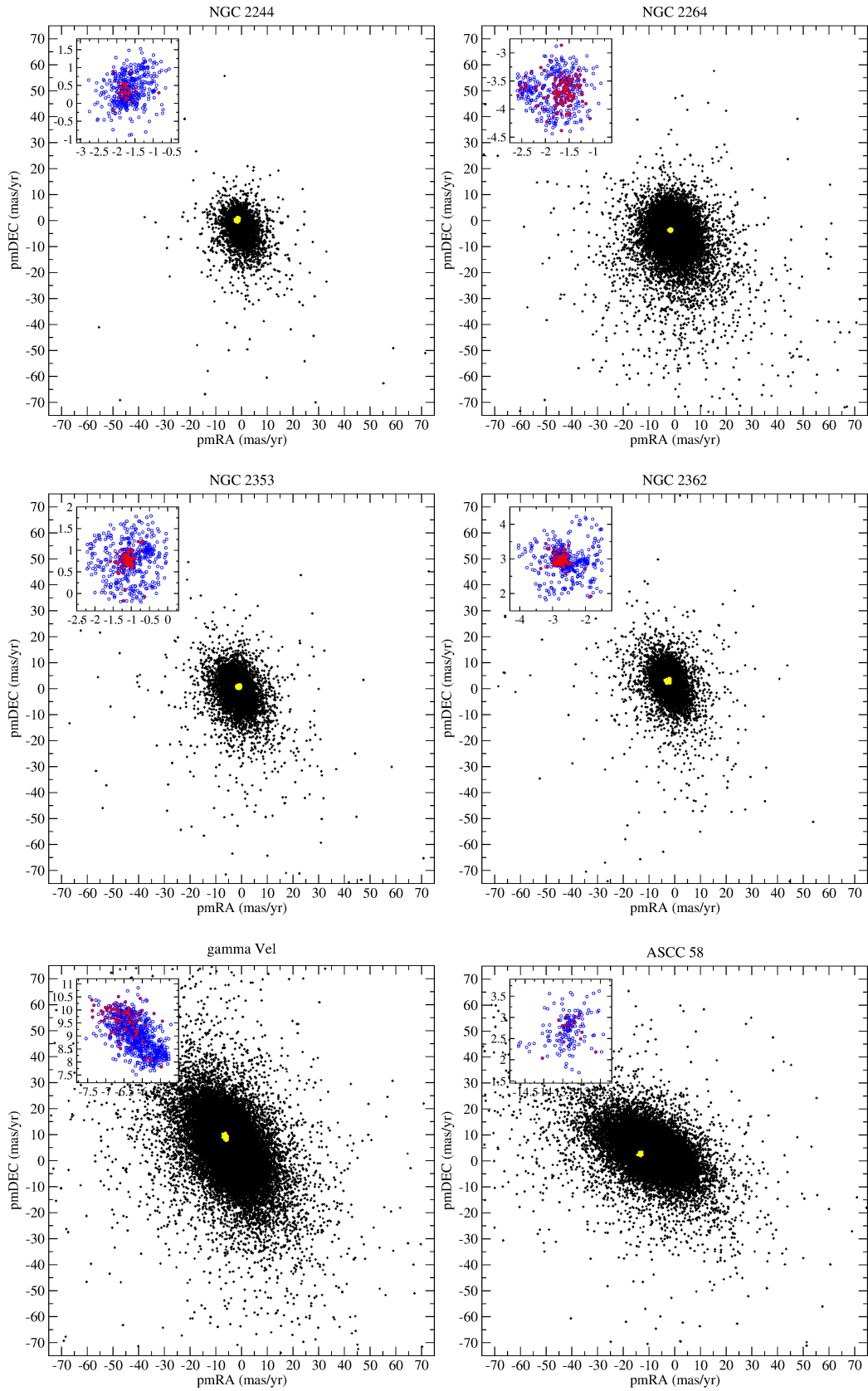
References

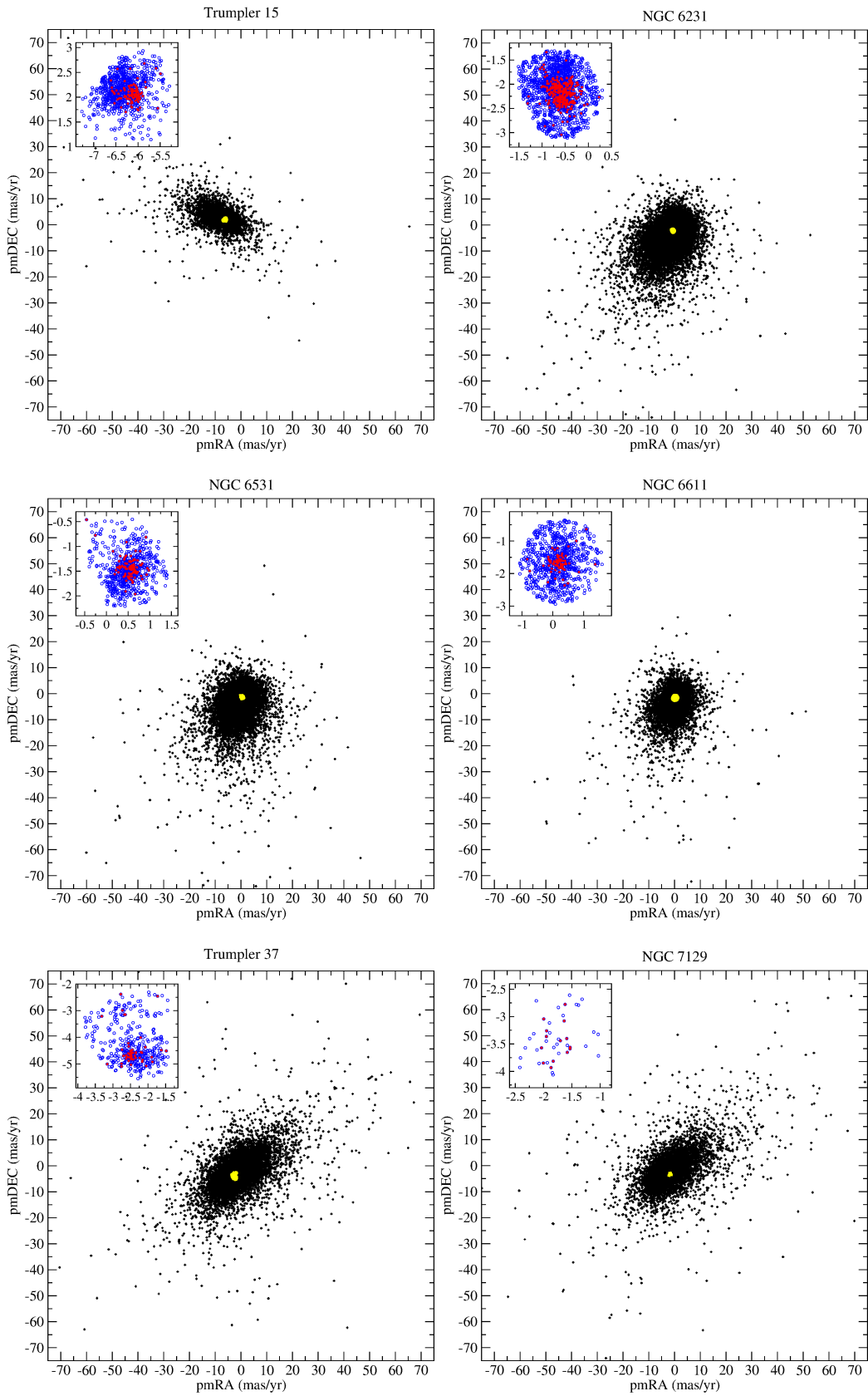
- Anders, F., Khalatyan, A., Queiroz, A. B. A., et al. 2022, *A&A*, 658, A91
 Anderson, K. R., Adams, F. C., & Calvet, N. 2013, *ApJ*, 774, 9
 Ansdell, M., Williams, J. P., Manara, C. F., et al. 2017, *AJ*, 153, 240
 Bailer-Jones, A. J. L., Rybizki, J., Fouvras, M., Demleitner, M., & Andrae, R. 2021, *AJ*, 161, 147
 Balaguer-Núñez, L., López del Fresno, M., Solano, E., et al. 2020, *MNRAS*, 492, 5811
 Balog, Z., Siegler, N., Rieke, G. H., et al. 2016, *ApJ*, 832, 87
 Bressan, A., Marigo, P., Girardi, L., et al. 2012, *MNRAS*, 427, 127
 Cantat-Gaudin, T. & Anders, F. 2020, *A&A*, 633, A99
 Casagrande, L., Lin, J., Rains, A. D., et al. 2021, *MNRAS*, 507, 2684
 Currie, T. & Sicilia-Aguilar, A. 2011, *ApJ*, 732, 24
 Desch, S. J., Kalyaan, A., & O'D. Alexander, C. M. 2018, *ApJS*, 238, 11
 Dias, W. S., Alessi, B. S., Moitinho, A., & Lépine, J. R. D. 2002, *A&A*, 389, 871
 El-Badry, K., Rix, H.-W., & Heintz, T. M. 2021, *MNRAS*, 506, 2269
 Ercoleo, B. & Pascucci, I. 2017, *Royal Society Open Science*, 4, 170114
 Fedele, D., van den Ancker, M. E., Henning, T., Jayawardhana, R., & Oliveira, J. M. 2010, *A&A*, 510, A72
 Fiorellino, E., Manara, C. F., Nisini, B., et al. 2021, *A&A*, 650, A43
 Gaia Collaboration, Brown, A. G. A., Vallenari, A., et al. 2021, *A&A*, 649, A1
 Gaia Collaboration, Prusti, T., de Bruijne, J. H. J., et al. 2016, *A&A*, 595, A1
 Getman, K. V., Feigelson, E. D., & Kuhn, M. A. 2014a, *ApJ*, 787, 109
 Getman, K. V., Feigelson, E. D., Kuhn, M. A., et al. 2018, *MNRAS*, 476, 1213
 Getman, K. V., Feigelson, E. D., Kuhn, M. A., et al. 2014b, *ApJ*, 787, 108
 Großschedl, J. E., Alves, J., Meingast, S., & Herbst-Kiss, G. 2021, *A&A*, 647, A91
 Guarcello, M. G., Biazzo, K., Drake, J. J., et al. 2021, *A&A*, 650, A157
 Gutermuth, R. A., Myers, P. C., Megeath, S. T., et al. 2008, *ApJ*, 674, 336
 Haich, Jr., K. E., Lada, E. A., & Lada, C. J. 2001, *ApJ*, 553, L153
 Hernández, J., Hartmann, L., Calvet, N., et al. 2008, *ApJ*, 686, 1195
 Hernández, J., Hartmann, L., Megeath, T., et al. 2007, *ApJ*, 662, 1067
 Hernández, J., Morales-Calderon, M., Calvet, N., et al. 2010, *ApJ*, 722, 1226
 Jeffries, R. D. 2017, *Mem. Soc. Astron. Italiana*, 88, 637
 Kharchenko, N. V., Piskunov, A. E., Schilbach, E., Röser, S., & Scholz, R. D. 2013, *A&A*, 558, A53
 Koenig, X. P. & Leisawitz, D. T. 2014, *ApJ*, 791, 131
 Kuhn, M. A., Hillenbrand, L. A., Sills, A., Feigelson, E. D., & Getman, K. V. 2019, *ApJ*, 870, 32
 Lada, C. J. & Adams, F. C. 1992, *ApJ*, 393, 278
 Lindgren, L., Klioner, S. A., Hernández, J., et al. 2021, *A&A*, 649, A2
 Mamajek, E. E. 2009, in *American Institute of Physics Conference Series*, Vol. 1158, *Exoplanets and Disks: Their Formation and Diversity*, ed. T. Usuda, M. Tamura, & M. Ishii, 3–10
 Meingast, S., Alves, J., & Rottensteiner, A. 2021, *A&A*, 645, A84
 Muzerolle, J., Allen, L. E., Megeath, S. T., Hernández, J., & Gutermuth, R. A. 2010, *ApJ*, 708, 1107
 Panja, A., Chen, W. P., Dutta, S., et al. 2021, *ApJ*, 910, 80
 Parker, R. J., Alcock, H. L., Nicholson, R. B., Panić, O., & Goodwin, S. P. 2021, *ApJ*, 913, 95
 Pfalzner, S., Steinhausen, M., & Menten, K. 2014, *ApJ*, 793, L34
 Prisinzano, L., Damiani, F., Kalari, V., et al. 2019, *A&A*, 623, A159
 Ribas, Á., Bouy, H., & Merín, B. 2015, *A&A*, 576, A52

- Richert, A. J. W., Feigelson, E. D., Getman, K. V., & Kuhn, M. A. 2015, *ApJ*, 811, 10
- Riello, M., De Angeli, F., Evans, D. W., et al. 2021, *A&A*, 649, A3
- Saurin, T. A., Bica, E., & Bonatto, C. 2012, *MNRAS*, 421, 3206
- Schiller, M., Bizzarro, M., & Fernandes, V. A. 2018, *Nature*, 555, 507
- Skrutskie, M. F., Cutri, R. M., Stiening, R., et al. 2006, *AJ*, 131, 1163
- Taylor, M. B. 2005, in *Astronomical Society of the Pacific Conference Series*, Vol. 347, *Astronomical Data Analysis Software and Systems XIV*, ed. P. Shopbell, M. Britton, & R. Ebert, 29
- van Terwisga, S. E., Hacar, A., & van Dishoeck, E. F. 2019, *A&A*, 628, A85
- Vincke, K. & Pfalzner, S. 2018, *ApJ*, 868, 1
- Wang, J., Feigelson, E. D., Townsley, L. K., et al. 2011, *ApJS*, 194, 11
- Wilking, B. A., Meyer, M. R., Greene, T. P., Mikhail, A., & Carlson, G. 2004, *AJ*, 127, 1131
- Wright, N. J. 2020, *New A Rev.*, 90, 101549
- Yasui, C., Kobayashi, N., Tokunaga, A. T., & Saito, M. 2014, *MNRAS*, 442, 2543
- Young, K. E., Young, C. H., Lai, S.-P., Dunham, M. M., & Evans, Neal J., I. 2015, *AJ*, 150, 40

Appendix A: Results. Figures and tables







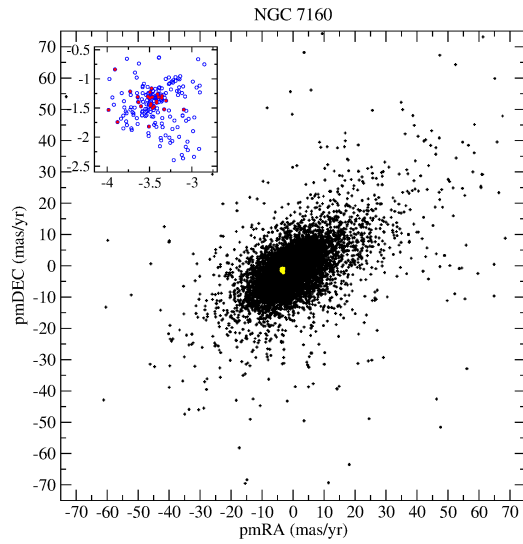
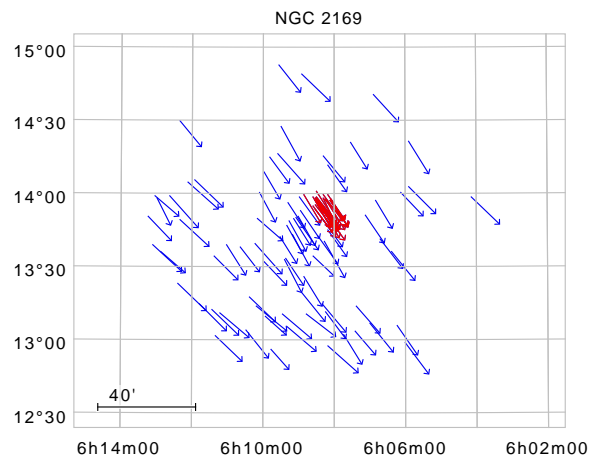
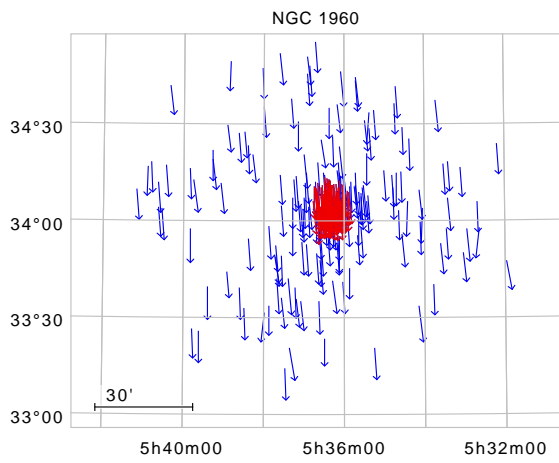
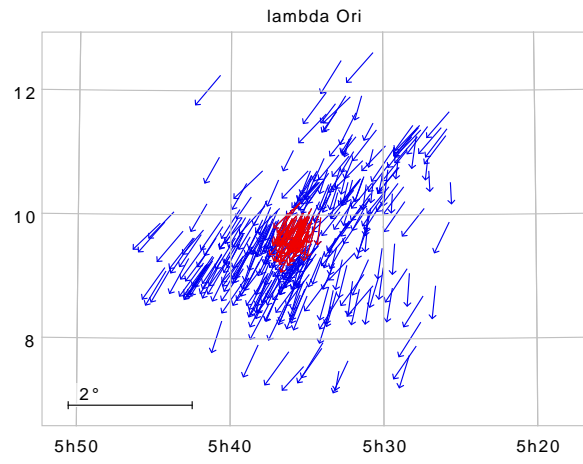
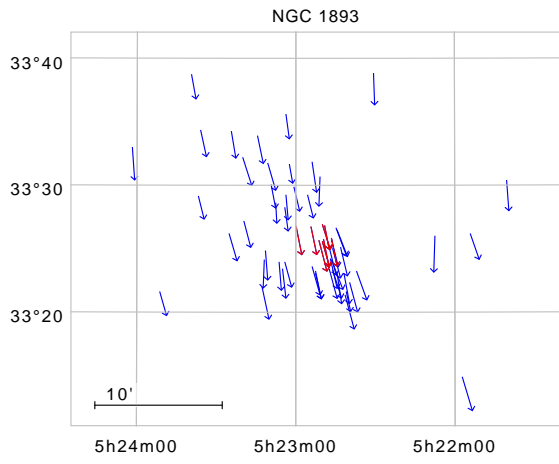
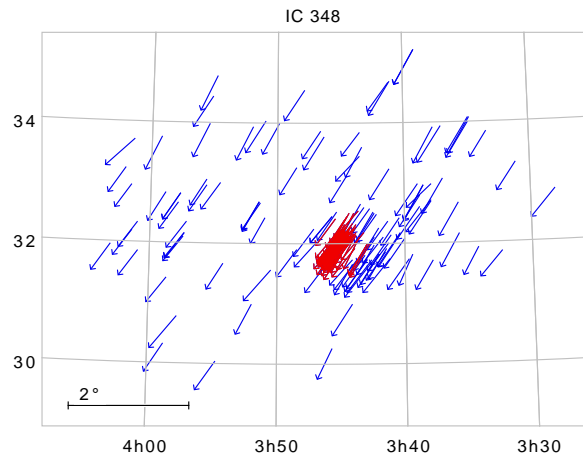
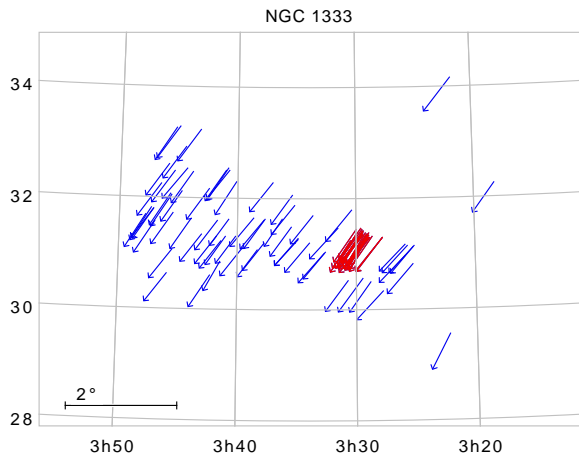
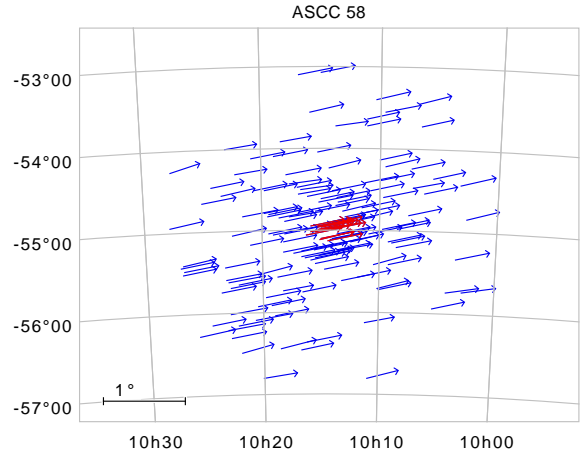
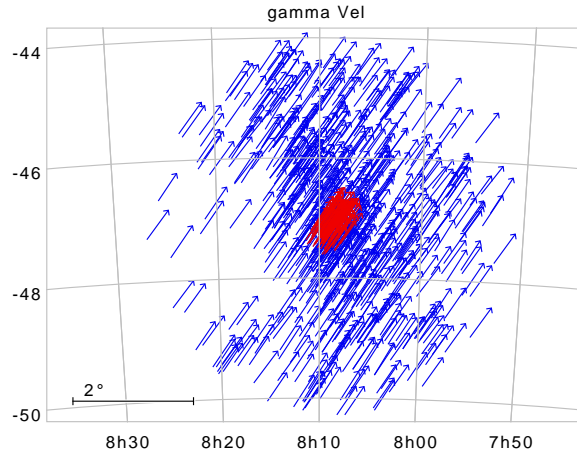
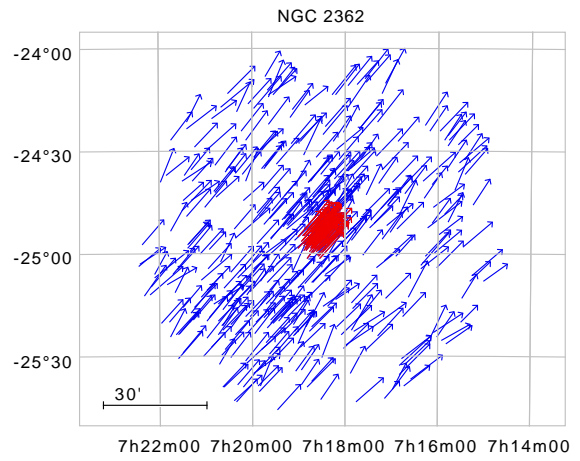
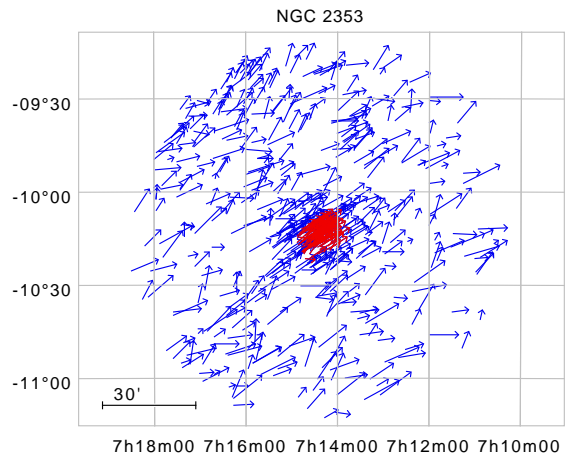
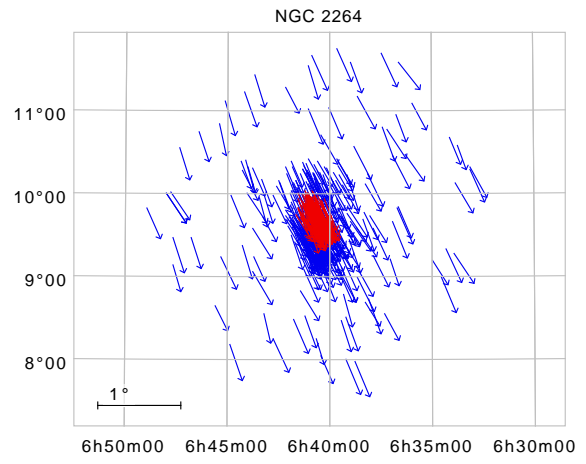
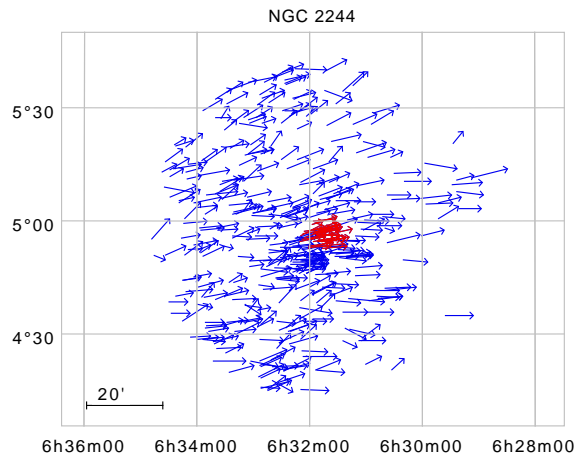
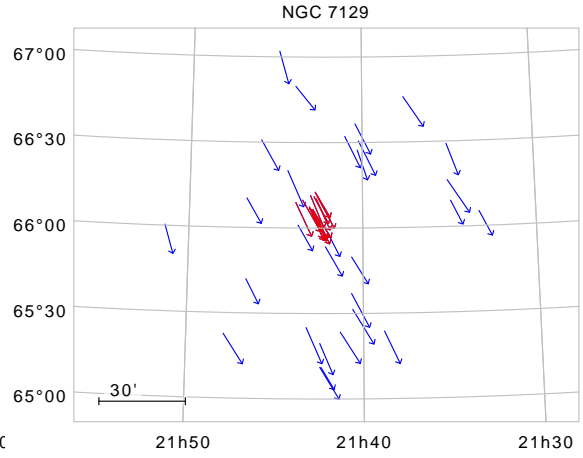
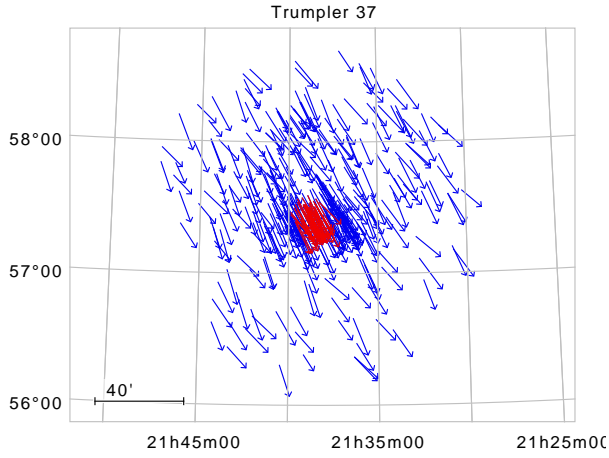
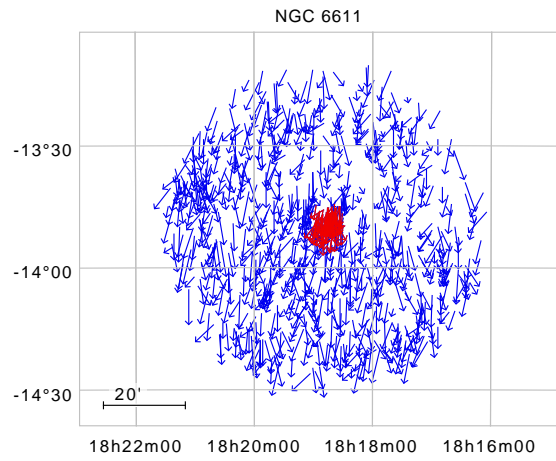
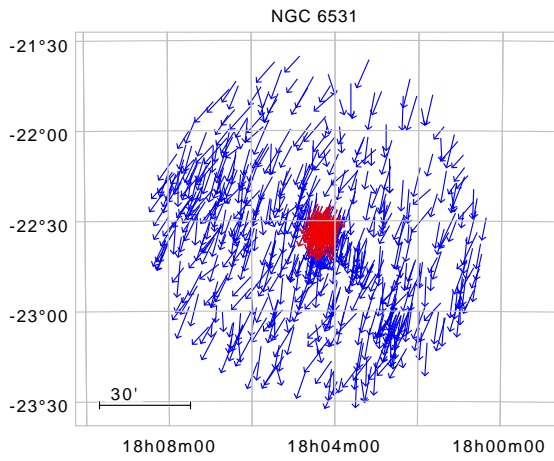
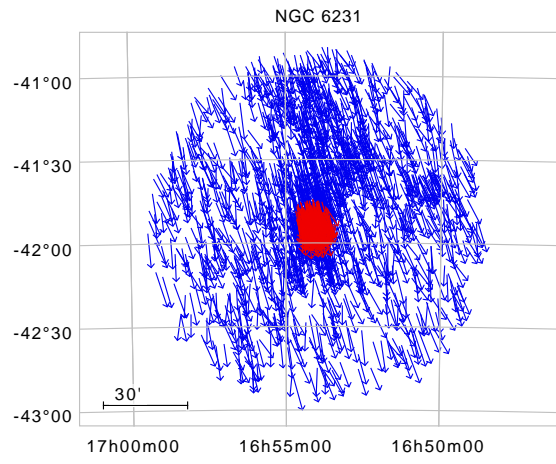
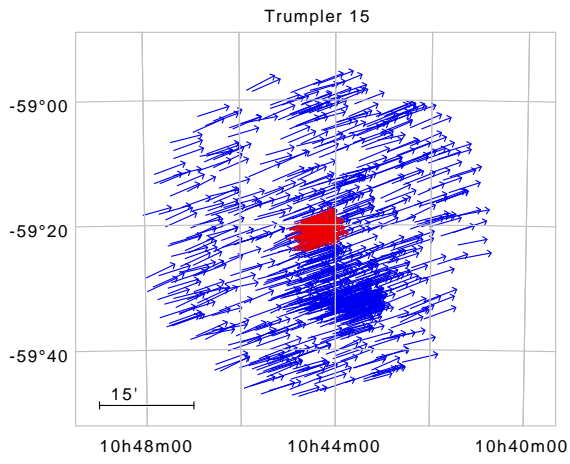


Fig. A.1: Proper motion distributions for the different clusters where the field stars within FOV_{20pc} having absolute proper motions $\leq 75 \text{ mas yr}^{-1}$ and the member stars are indicated in black and yellow, respectively. The top left sub-panels focus on the proper motions of the members, where the blue and red circles correspond to those identified within FOV_{20pc} and FOV_{2pc} , respectively. Typical (mean) uncertainties in proper motions are $\sim 0.04 \text{ mas yr}^{-1}$, roughly comparable to the size of such circles for most cases.







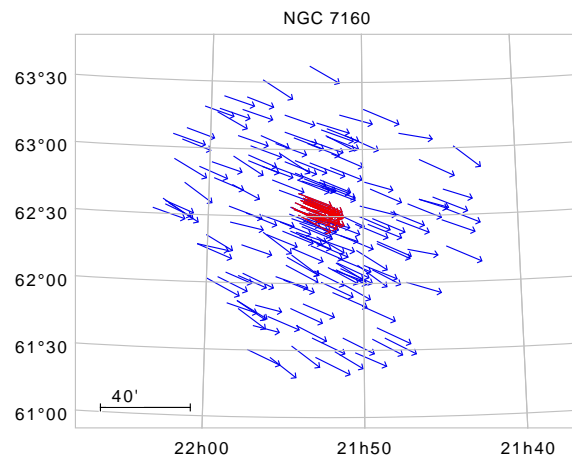
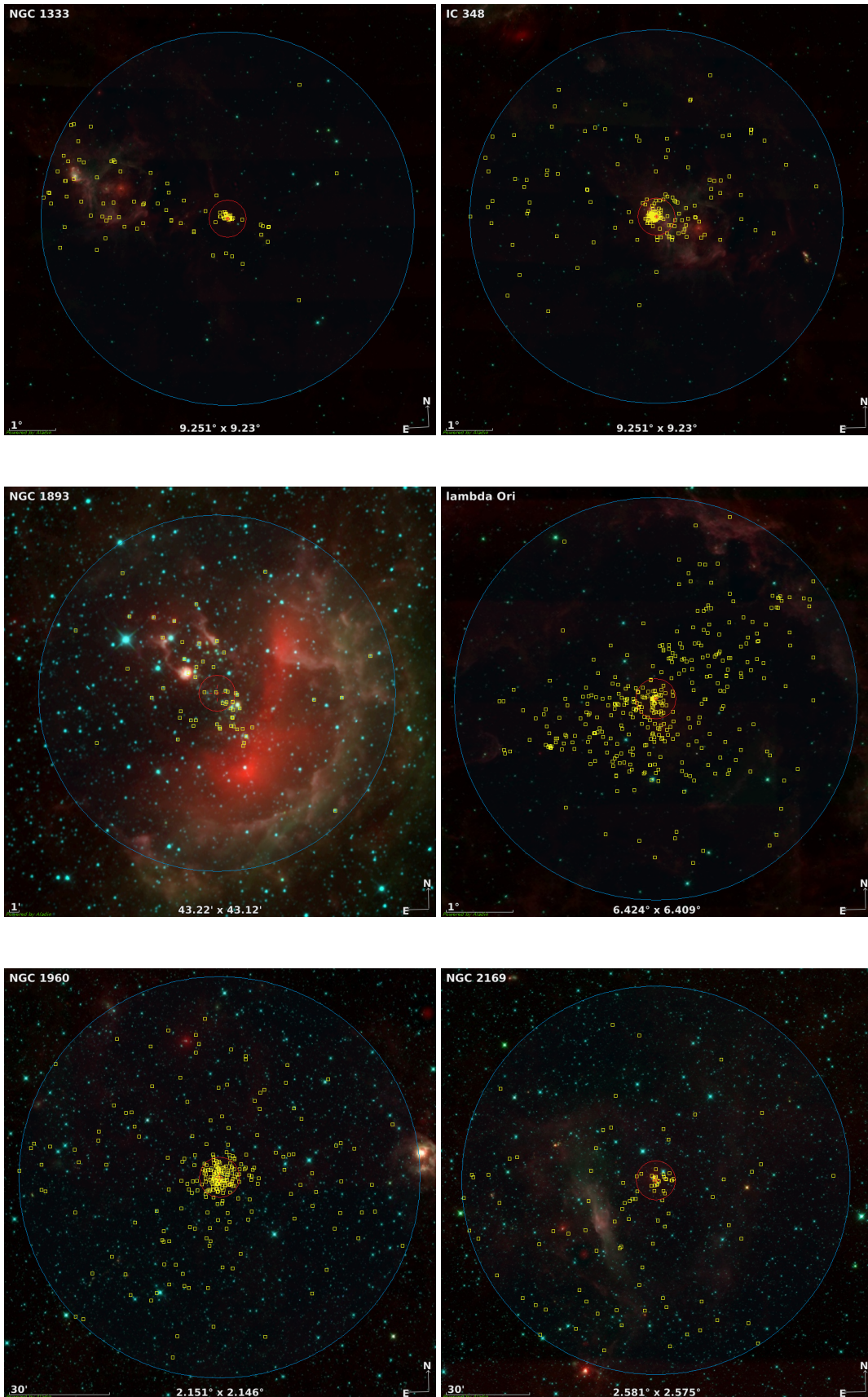
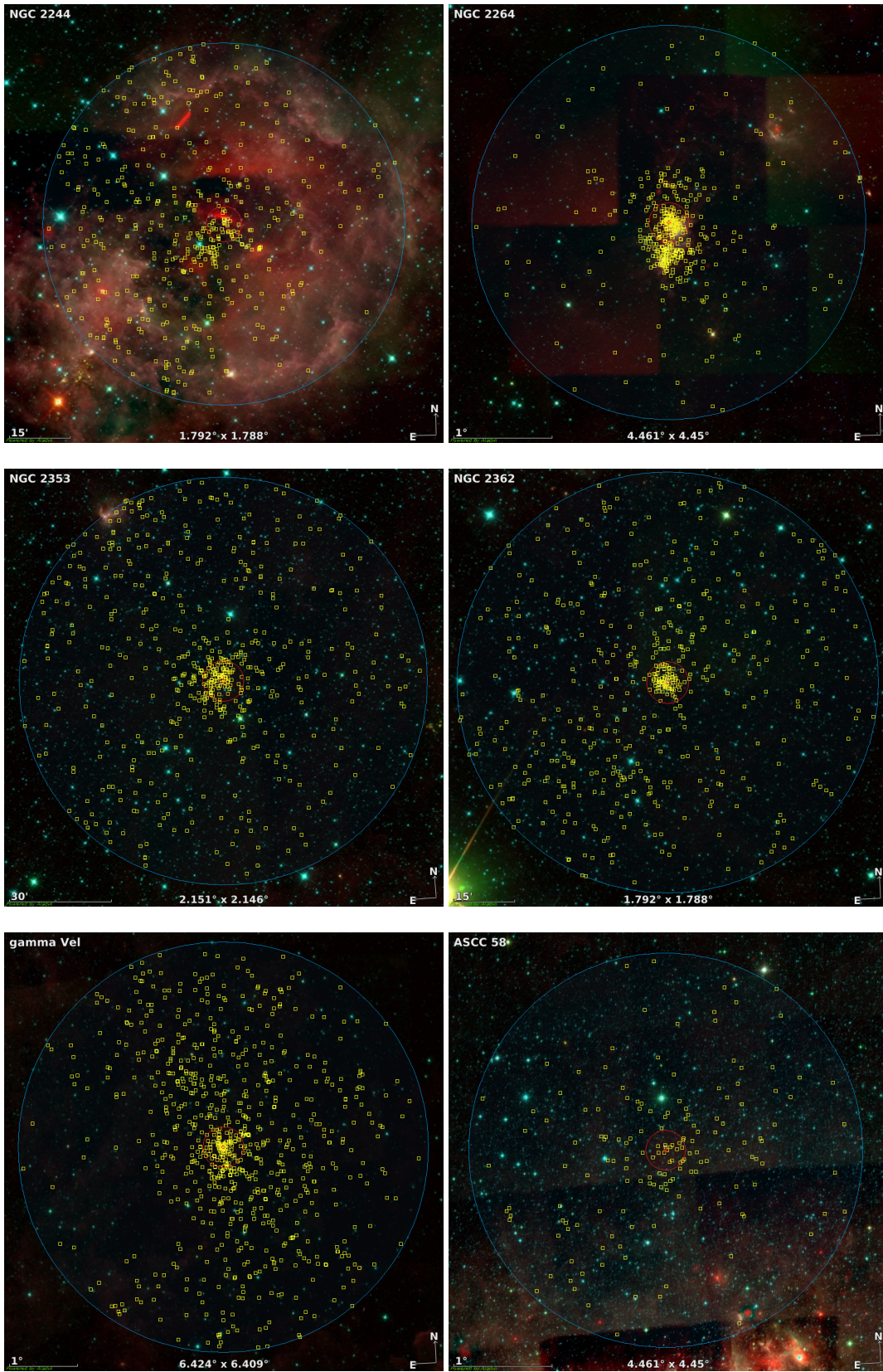
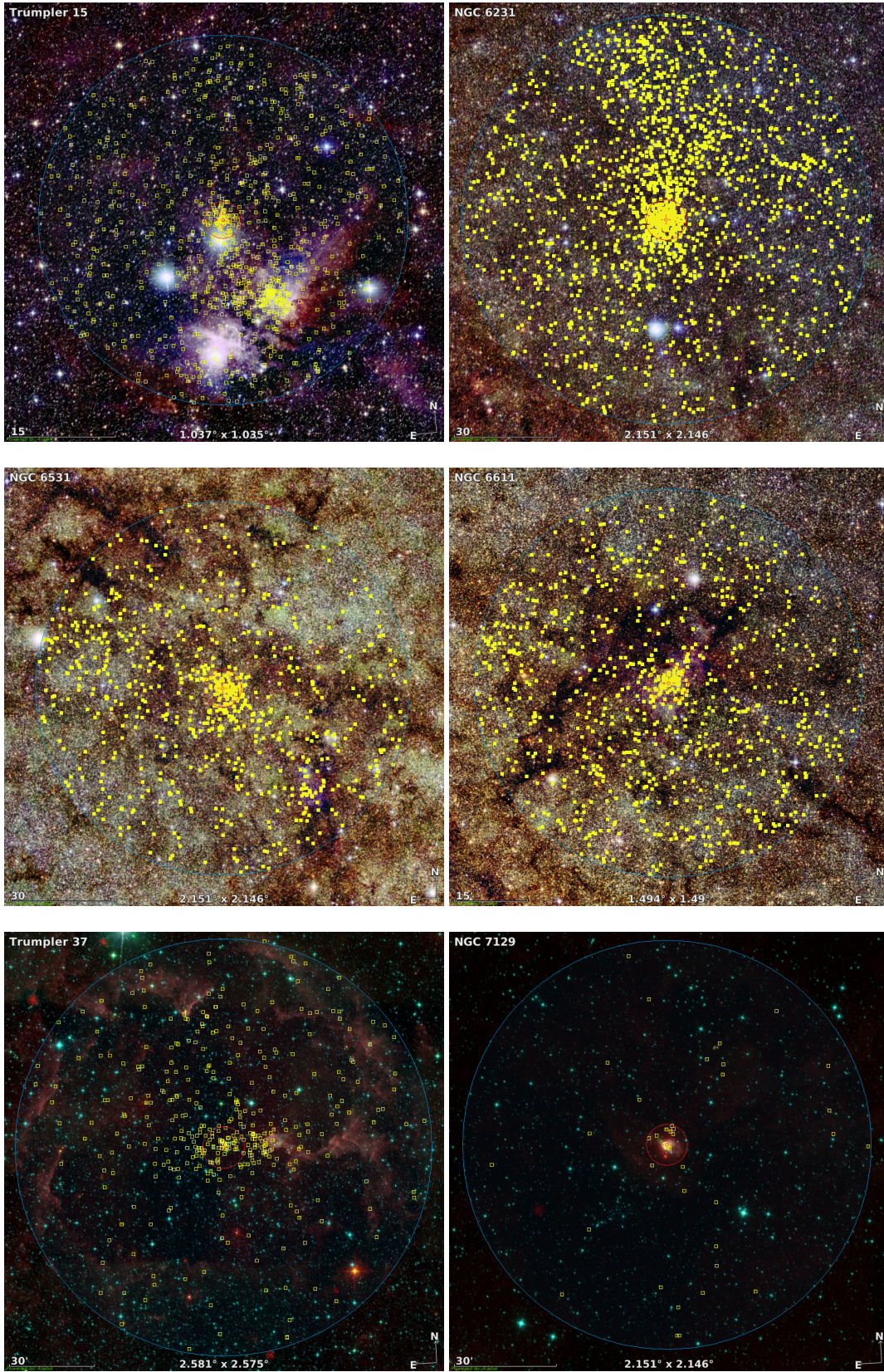


Fig. A.2: Sky projections (North to the top and East to the left) for the different clusters where the blue and red arrows indicate the directions of motion of all members identified within FOV_{20pc} and FOV_{2pc} , respectively.







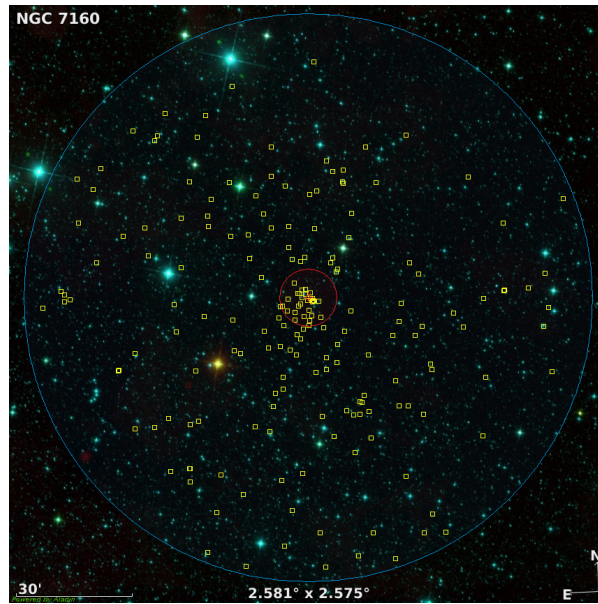
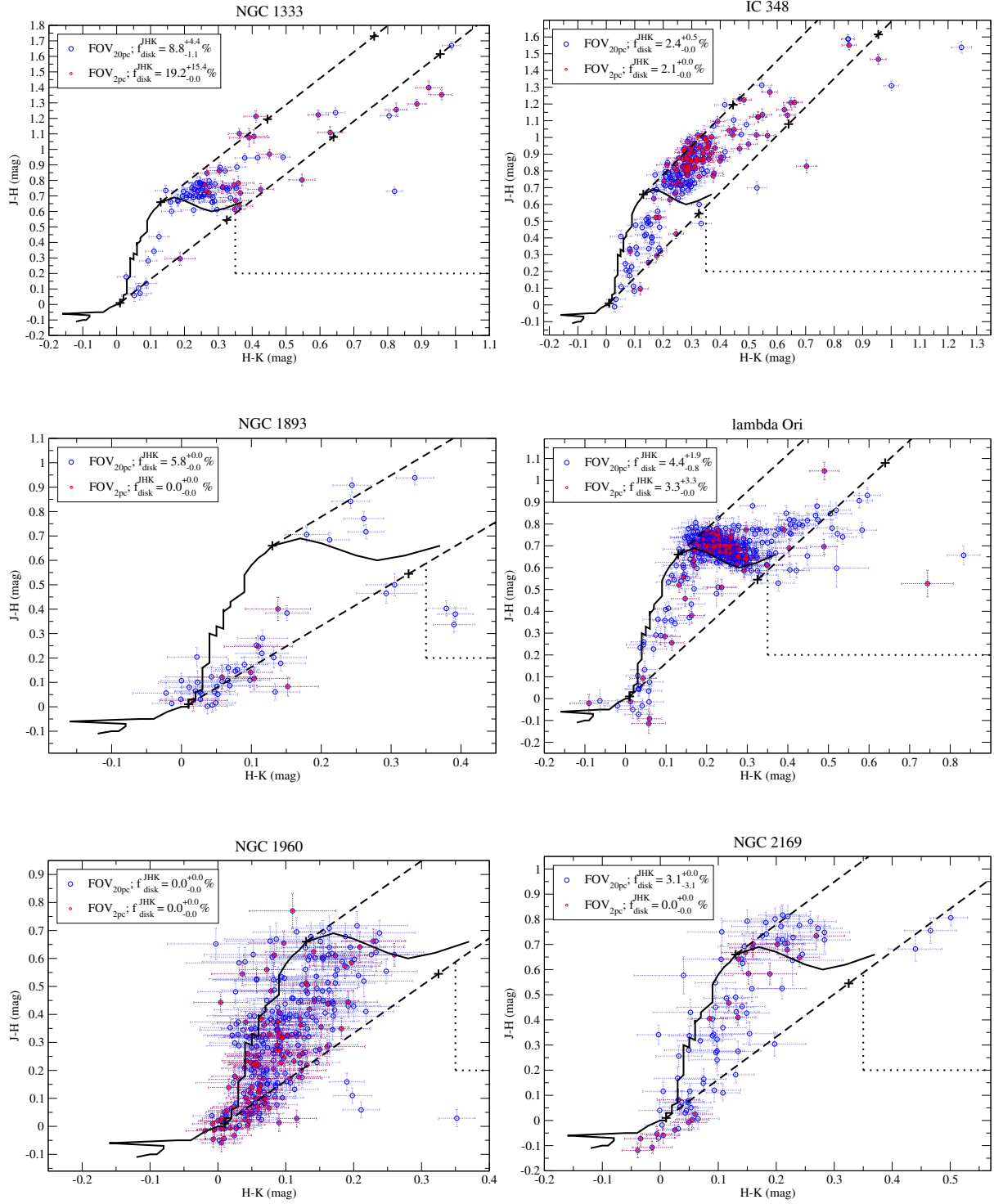
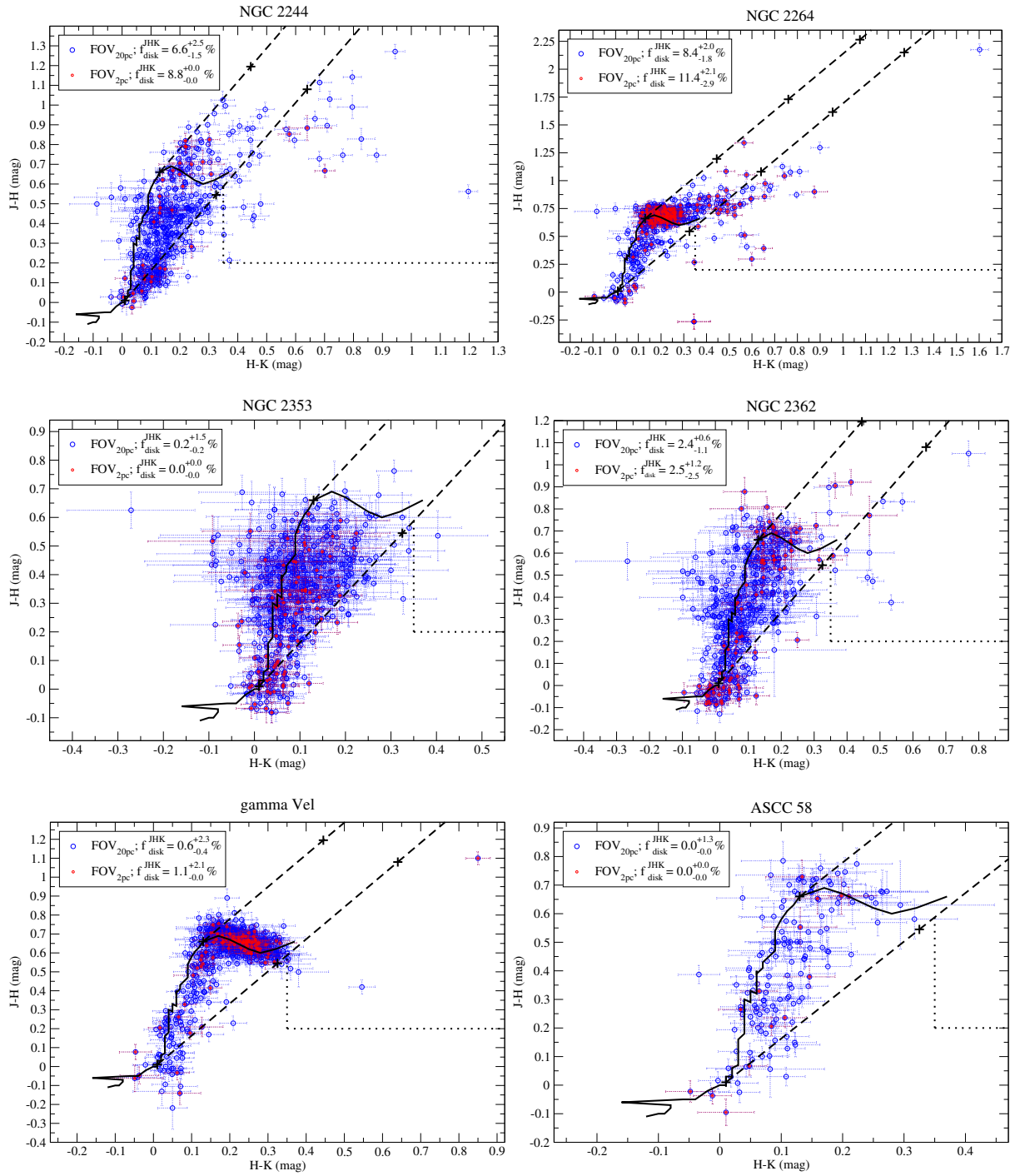
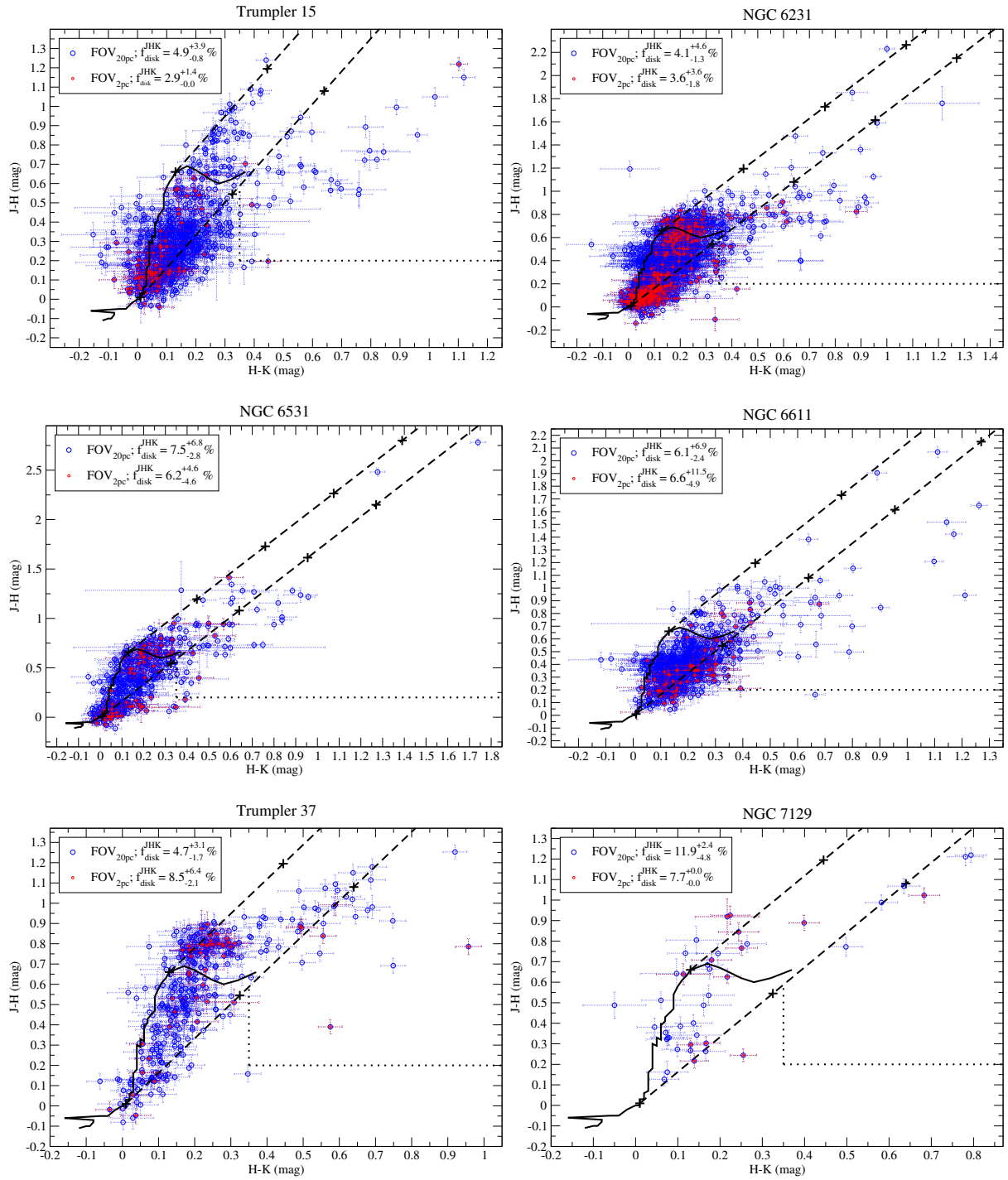


Fig. A.3: Sky projections for the different clusters where the yellow squares indicate the positions of all members identified within FOV_{20pc} and FOV_{2pc} , whose corresponding sizes are indicated with the blue and red circles, respectively. Background images are colored according to the ALLWISE W1, W2, and W4 bands (except for Trumpler 15, NGC 6231, NGC 6531, and NGC 6611, where 2MASS images are used for a better visualization).







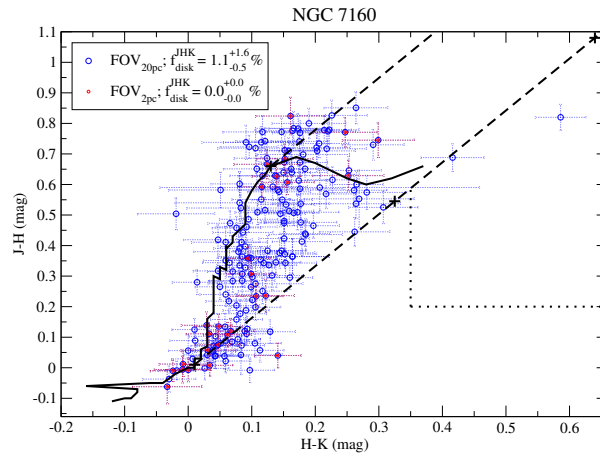
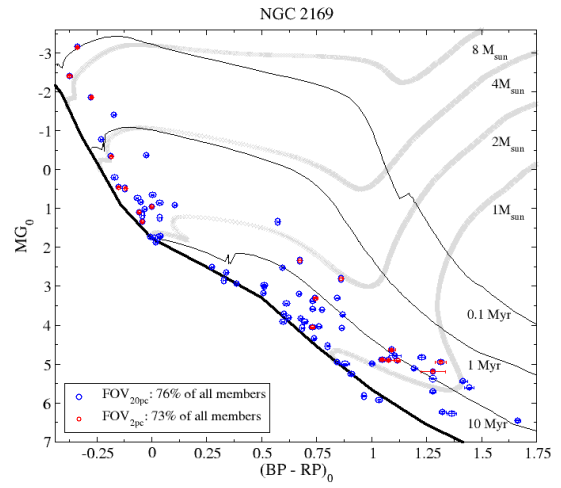
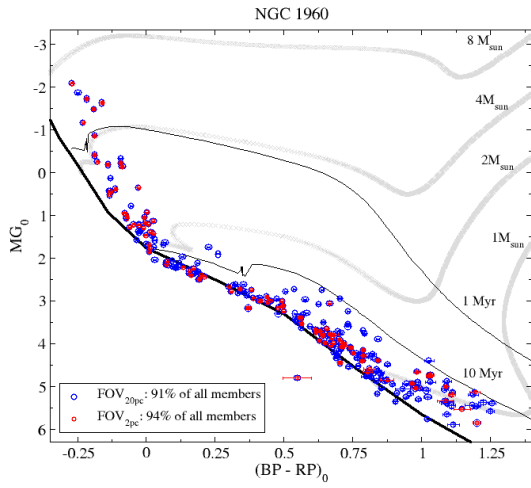
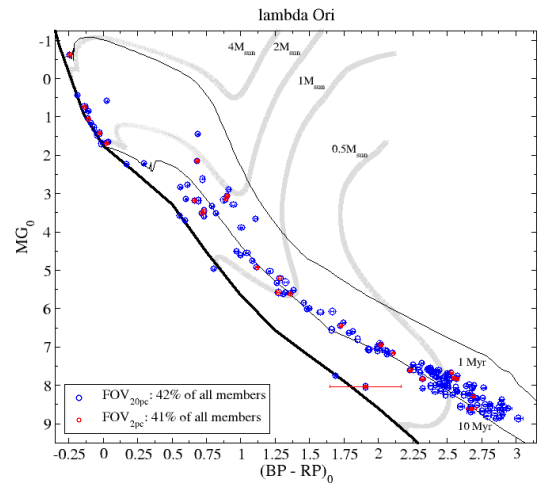
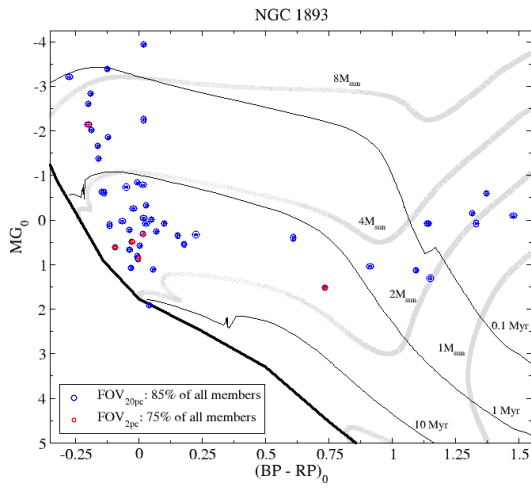
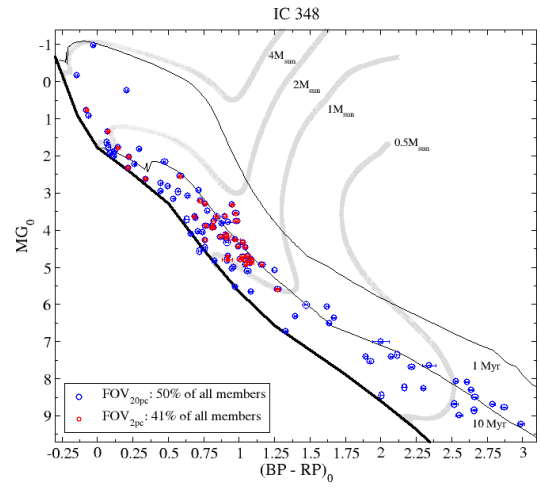
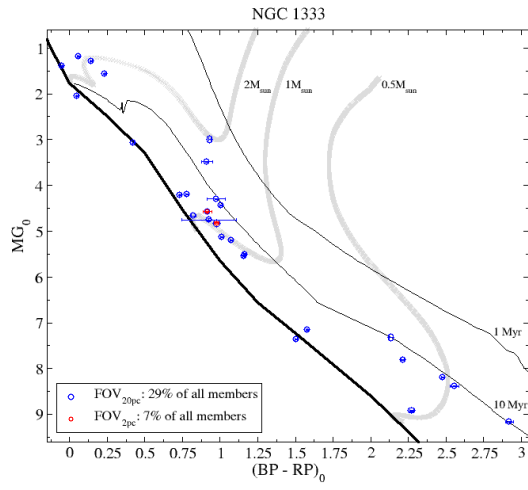
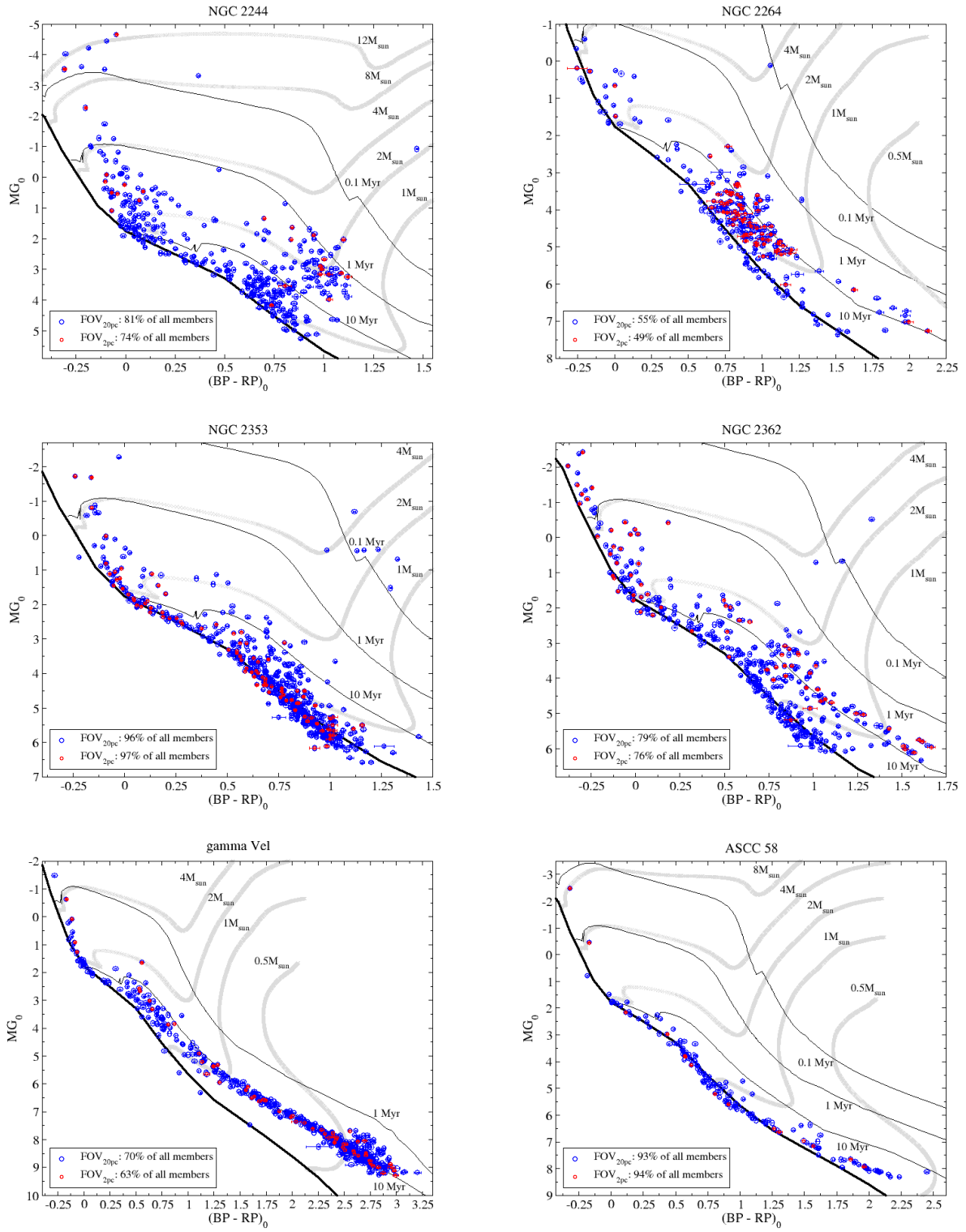
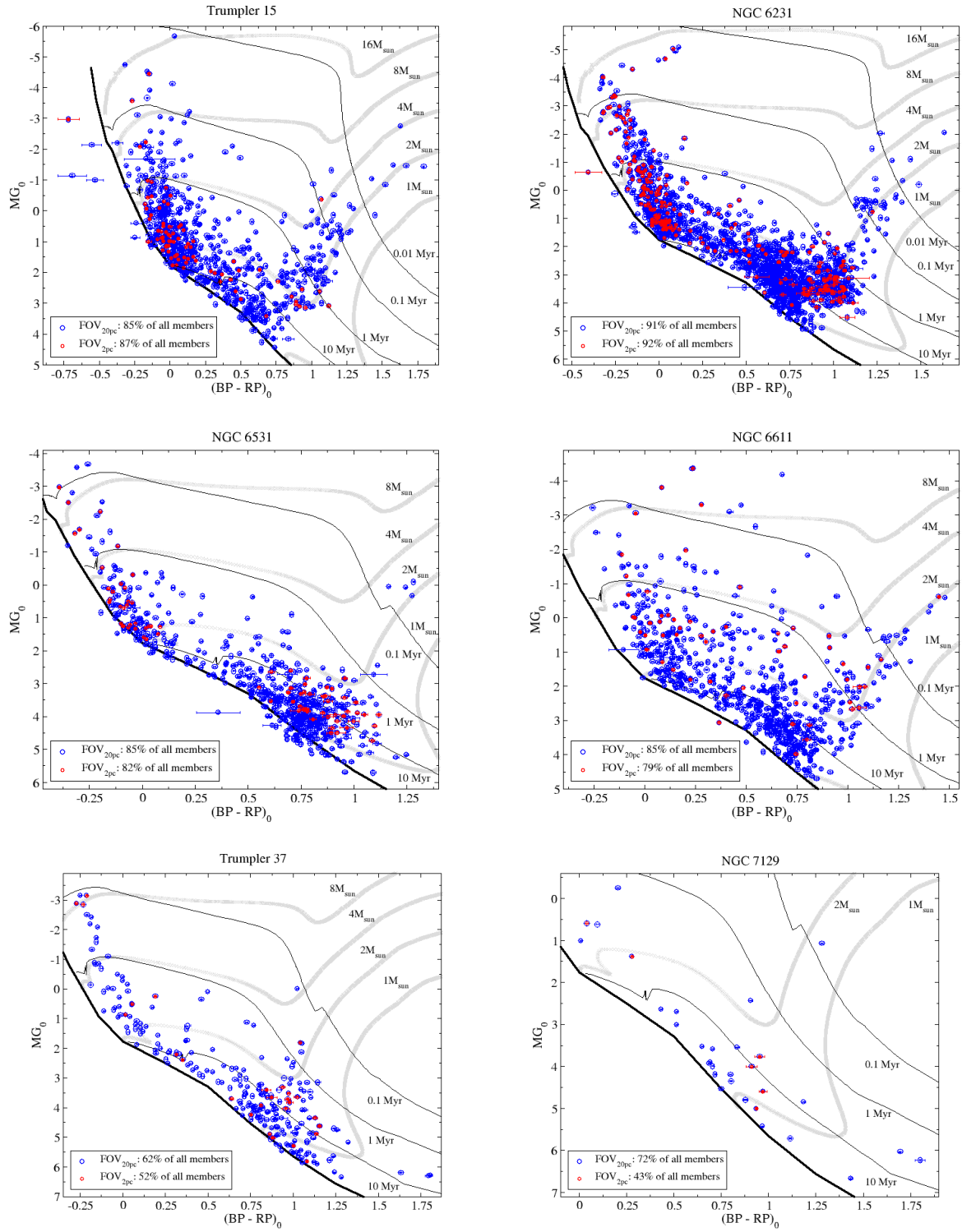


Fig. A.4: JHK color-color diagrams for the different clusters. In each panel, the solid line represents the expected position of non-extinguished MS stars in the diagram, and the dashed lines the direction of the extinction vector and thus the rough boundaries for extinguished MS stars (crosses within the dashed lines indicate an optical extinction increase of 5 magnitudes). Sources located to the right of the right hand dashed line and within the dotted lines are considered disk stars. Inner disk fractions are indicated in the legends, as inferred from all identified members within FOV_{20pc} and within FOV_{2pc} (blue and red symbols, respectively)







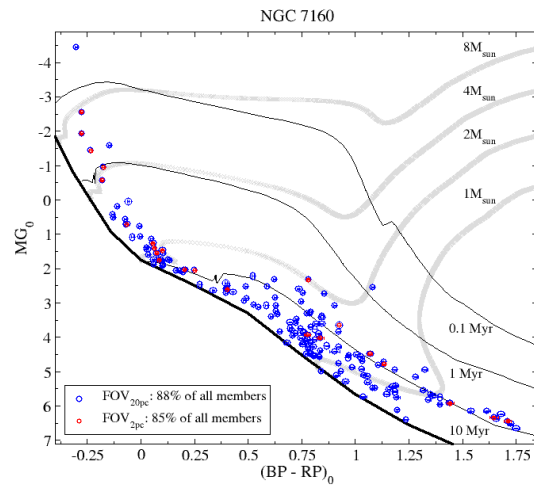


Fig. A.5: Extinction corrected Gaia CMDs for the different clusters. The ZAMS loci is indicated with the black solid curve. PMS isochrones and evolutionary tracks from Bressan et al. (2012) are overplotted in black and gray for the stellar ages and masses indicated. The representativeness of the diagrams is limited to the fraction of all members identified within FOV_{20pc} and FOV_{2pc} having optical extinction estimates in Anders et al. (2022), which is indicated in the legends.

Table A.1: Young Stellar Clusters. Regions and membership

Name	FOV _{20pc}			FOV _{2pc}								
	RA _{cent} (°)	DEC _{cent} (°)	R (′)	N _{memb} /N _{tot}	π (mas)	pmRA (mas yr ⁻¹)	pmDEC (mas yr ⁻¹)	R (′)	N _{memb} /N _{tot}	π (mas)	pmRA (mas yr ⁻¹)	pmDEC (mas yr ⁻¹)
NGC 1333	52.2968	31.3097	240	95/43277	3.40±0.08	6.94±0.73	-9.37±0.67	24	28/244	3.39±0.08	7.00±0.80	-9.79±0.46
IC 348	56.0608	32.1560	240	209/53819	3.15±0.08	4.36±0.59	-6.30±0.64	24	97/312	3.14±0.06	4.48±0.53	-6.33±0.52
NGC 1893	80.7237	33.4438	18	59/922	0.32±0.04	-0.30±0.14	-1.41±0.17	1.8	8/22	0.31±0.03	-0.32±0.04	-1.38±0.12
λ Ori	83.7802	9.9091	180	377/55430	2.50±0.05	1.14±0.47	-2.06±0.30	18	63/577	2.50±0.05	1.00±0.41	-2.02±0.19
NGC 1960	84.0840	34.1350	60	273/9263	0.85±0.02	-0.21±0.15	-3.39±0.17	6	114/227	0.85±0.02	-0.21±0.14	-3.43±0.13
NGC 2169	92.1250	13.9510	70	102/10500	1.03±0.04	-1.25±0.25	-1.58±0.17	7	26/153	1.03±0.04	-1.10±0.13	-1.59±0.12
NGC 2244	97.9817	4.9390	44	418/4255	0.68±0.04	-1.65±0.38	0.39±0.41	4.4	35/75	0.67±0.04	-1.75±0.21	0.35±0.21
NGC 2264	100.2471	9.8755	120	452/32665	1.37±0.06	-1.78±0.38	-3.68±0.29	12	142/242	1.38±0.05	-1.68±0.30	-3.68±0.22
NGC 2353	108.6242	-10.2711	60	545/11452	0.82±0.08	-1.05±0.43	0.77±0.38	6	92/206	0.84±0.05	-1.09±0.16	0.76±0.20
NGC 2362	109.6658	-24.9557	52	485/12410	0.76±0.05	-2.61±0.46	2.93±0.39	5.2	90/212	0.77±0.03	-2.75±0.21	2.98±0.20
γ Vel	122.3831	-47.3366	180	810/134095	2.76±0.14	-6.20±0.44	9.08±0.64	18	99/1364	2.87±0.12	-6.48±0.40	9.53±0.56
ASCC 58	153.8180	-55.0003	120	160/99215	2.11±0.07	-13.42±0.48	2.70±0.38	12	16/1068	2.08±0.03	-13.32±0.31	2.71±0.28
Trumpler 15	161.1743	-59.3664	26	870/6216	0.40±0.04	-6.31±0.35	2.14±0.31	2.6	94/139	0.39±0.03	-6.13±0.21	2.08±0.18
NGC 6231	253.5356	-41.8284	60	1726/26977	0.60±0.04	-0.64±0.32	-2.12±0.38	6	265/546	0.60±0.04	-0.58±0.21	-2.19±0.22
NGC 6531	271.0576	-22.4935	55	696/15689	0.79±0.04	0.50±0.34	-1.46±0.34	5.5	91/257	0.80±0.04	0.54±0.21	-1.42±0.22
NGC 6611	274.6993	-13.8090	40	809/7796	0.59±0.05	0.16±0.53	-1.63±0.58	4	72/133	0.56±0.04	0.20±0.31	-1.66±0.27
Trumpler 37	324.7486	57.4782	73	381/18293	1.07±0.04	-2.43±0.52	-4.28±0.75	7.3	52/290	1.07±0.04	-2.43±0.33	-4.47±0.62
NGC 7129	325.7401	66.1140	60	43/8627	1.07±0.06	-1.77±0.33	-3.41±0.39	6	14/63	1.10±0.04	-1.77±0.18	-3.45±0.32
NGC 7160	328.4142	62.6020	72	190/20532	1.06±0.05	-3.42±0.23	-1.44±0.34	7.2	27/213	1.09±0.04	-3.51±0.19	-1.38±0.18

Notes. Columns 1 to 3 list the name of the cluster and the coordinates of its central position. Columns 4 to 8 refer to FOV_{20pc}, listing the associated angular radius, number of members identified divided by the total number of sources within the FOV having Gaia EDR3 proper motions and reliable parallaxes (as defined in Sect. 2.1), and inferred mean parallax and proper motions (uncertainties refer to the standard deviations). The rest of the columns are equivalent to the previous, but related to FOV_{2pc}.

Table A.2: Young Stellar Clusters. Members identified

RA °	DEC °	pmRA mas yr ⁻¹	pmDEC mas yr ⁻¹	π mas	BP mag	RP mag NGC 1333	G mag	d_{cent} °	PROB ...	H-K mag	J-H mag	disk? ...
55.6003	32.1583	6.96 ± 0.08	-9.56 ± 0.06	3.32 ± 0.06	18.651 ± 0.023	15.577 ± 0.006	16.846 ± 0.003	2.9348	1.000	0.26 ± 0.04	0.71 ± 0.04	
52.3399	31.3528	7.64 ± 0.06	-9.59 ± 0.05	3.41 ± 0.06	18.149 ± 0.015	14.594 ± 0.005	15.957 ± 0.003	0.0567	0.993	0.35 ± 0.04	0.67 ± 0.04	
52.1815	31.2934	7.27 ± 0.13	-9.74 ± 0.10	3.35 ± 0.12	19.312 ± 0.088	15.196 ± 0.034	16.805 ± 0.011	0.0998	0.980	0.82 ± 0.03	1.26 ± 0.04	
56.1558	32.1032	4.36 ± 0.05	-6.38 ± 0.03	3.10 ± 0.05	16.683 ± 0.013	14.011 ± 0.005	15.205 ± 0.003	0.0962	1.000	0.28 ± 0.03	0.94 ± 0.03	
55.3089	31.9961	4.58 ± 0.02	-6.08 ± 0.02	3.28 ± 0.02	12.590 ± 0.003	11.151 ± 0.004	11.945 ± 0.003	0.6569	1.000	0.18 ± 0.03	0.34 ± 0.03	
56.0903	32.1069	4.70 ± 0.07	-6.15 ± 0.05	3.12 ± 0.08	17.776 ± 0.024	14.688 ± 0.009	15.984 ± 0.003	0.0551	1.000	0.29 ± 0.03	0.93 ± 0.03	
80.6932	33.4024	-0.60 ± 0.03	-1.54 ± 0.02	0.30 ± 0.03	14.938 ± 0.003	13.667 ± 0.004	14.395 ± 0.003	0.0486	1.000	0.30 ± 0.04	0.50 ± 0.04	
80.6866	33.4435	-0.50 ± 0.03	-1.37 ± 0.02	0.34 ± 0.02	11.412 ± 0.003	11.000 ± 0.004	11.274 ± 0.003	0.0310	0.998	0.03 ± 0.03	0.05 ± 0.03	
80.6833	33.4407	-0.50 ± 0.03	-1.33 ± 0.02	0.37 ± 0.03	10.332 ± 0.003	9.940 ± 0.004	10.204 ± 0.003	0.0338	0.996	0.05 ± 0.03	0.02 ± 0.03	
						...						

Notes. Columns 1 to 10 list the Gaia EDR3 coordinates, proper motions, parallax, BP, RP and G magnitudes, angular distance to the center of the cluster, and membership probability (ordered from higher to lower) of each member identified (PROB > 0) within FOV_{20pc}. The members within FOV_{2pc} can be retrieved from d_{cent} and the corresponding angular radius (see Col. 9 in Table A.1). Columns 11 and 12 list the 2MASS colors, when available. Objects identified as disk stars or potential disk stars based on the JHK colors and errorbars are tagged with "yes" and "yes.?" in the last column. The absence of such tags does not necessarily mean that the star is diskless (Sects. 2.2 and 4.2). Only the three first rows for the three first clusters are shown. A complete version of this table is available online.

Appendix B: Virtual Observatory compliant, online catalogue

In order to help the astronomical community on using the information obtained in this paper, we developed an archive system that can be accessed from a webpage³ or through a Virtual Observatory ConeSearch⁴.

The archive system implements a very simple search interface that allows queries by coordinates and radius as well as by cluster name and other parameters of interest. The user can also select the maximum number of sources (with values from 10 to unlimited). The result of the query is a HTML table with all the sources found in the archive fulfilling the search criteria. The result can also be downloaded as a VOTable or a CSV file. Detailed information on the output fields can be obtained placing the mouse over the question mark located close to the name of the column. The archive also implements the SAMP⁵ (Simple Application Messaging) Virtual Observatory protocol. SAMP allows Virtual Observatory applications to communicate with each other in a seamless and transparent manner for the user. This way, the results of a query can be easily transferred to other VO applications, such as, for instance, Topcat (Taylor 2005).

Appendix C: Comparison with previous Gaia-based results

Figure C.1 compares our results with those in Cantat-Gaudin & Anders (2020), which provides a complete Gaia DR2-based census of Galactic clusters including all analysed here. Cantat-Gaudin & Anders (2020) reported the use of FOVs significantly larger than in the previous reference papers by Dias et al. (2002) and Kharchenko et al. (2013), although the specific sizes were not systematically listed. Based on the positions of the members located furthest from the clusters' centers, a reasonable estimate of the FOVs used in Cantat-Gaudin & Anders (2020) can be derived. Such FOVs, as well as the total number of potential members (i.e. with non-null membership probability) from Cantat-Gaudin & Anders (2020), are compared to those from this work in the top left panel of Fig. C.1. Our FOV_{20pc} and number of potential members are ~ 4.3 and ~ 1.4 times larger on average. It is noted that this is a rough comparison that does not take into account the different methodologies for membership identification or the limiting magnitudes considered. In this particular, although Cantat-Gaudin & Anders (2020) probed more sources by including stars 1 Gaia G-magnitude fainter than here, we still identify a larger number of members for the majority of the clusters because of the use of a larger FOV. The rest of the panels in Fig. C.1 compare the parallaxes and proper motions. Values and errorbars refer to the means and standard deviations derived from FOV_{20pc} (see Table A.1) and to the ones tabulated in Cantat-Gaudin & Anders (2020). Despite of the above mentioned differences concerning methodologies, FOVs, and the number of members identified, parallaxes and proper motions coincide within $\pm 1\sigma$ for all clusters. Mean distances to each cluster were derived from the ones of all members within FOV_{20pc} , based on the parallax-distance geometrical transformation in Bailer-Jones et al. (2021). Distances are indicated in the

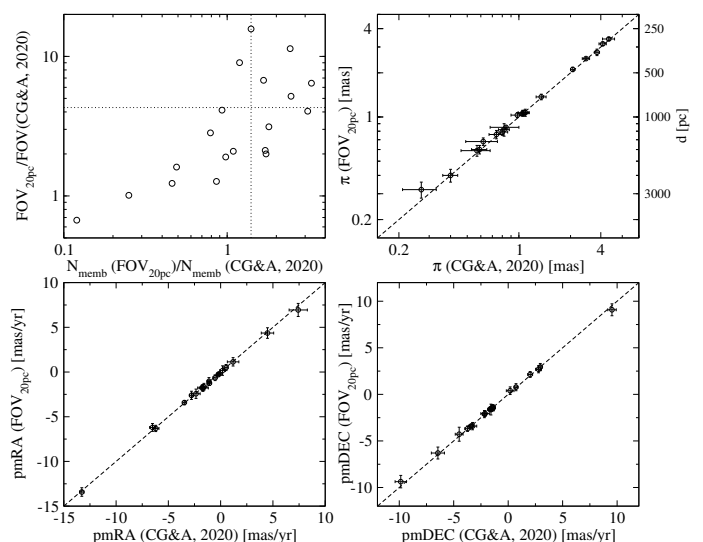


Fig. C.1: Comparison between data from this work and from Cantat-Gaudin & Anders (2020) (Top left): ratio between the FOVs used versus ratio between the total number of members identified. The dotted lines indicate the typical (mean) values in each axis. (Top right, bottom left, and bottom right): Comparison between parallaxes and proper motions. The dashed lines indicate equal values. Distances are indicated in the opposite y-axis of the top right panel for reference.

top right panel of Fig. C.1, and were listed in Table 1 along with the corresponding standard deviations.

³ <http://svocats.cab.inta-csic.es/diskfrac>

⁴ e.g. <http://svocats.cab.inta-csic.es/diskfrac/cs.php?RA=152.799&DEC=-54.423&SR=0.1&VERB=2>

⁵ <http://www.ivoa.net/documents/SAMP>